

Origin of the synergistic effect between TiO₂ crystalline phases in the Ni/TiO₂-catalyzed CO₂ methanation reaction

Messou, Davina; Bernardin, Vincent; Meunier, Frédéric; Ordoño, Marta Borges; Urakawa, Atsushi; Machado, Bruno F.; Collière, Vincent; Philippe, Régis; Serp, Philippe; Le Berre, Carole

DOI

[10.1016/j.jcat.2021.04.004](https://doi.org/10.1016/j.jcat.2021.04.004)

Publication date

2021

Document Version

Accepted author manuscript

Published in

Journal of Catalysis

Citation (APA)

Messou, D., Bernardin, V., Meunier, F., Ordoño, M. B., Urakawa, A., Machado, B. F., Collière, V., Philippe, R., Serp, P., & Le Berre, C. (2021). Origin of the synergistic effect between TiO₂ crystalline phases in the Ni/TiO₂-catalyzed CO₂ methanation reaction. *Journal of Catalysis*, 398, 14-28. ²
<https://doi.org/10.1016/j.jcat.2021.04.004>

Important note

To cite this publication, please use the final published version (if applicable).
Please check the document version above.

Copyright

Other than for strictly personal use, it is not permitted to download, forward or distribute the text or part of it, without the consent of the author(s) and/or copyright holder(s), unless the work is under an open content license such as Creative Commons.

Takedown policy

Please contact us and provide details if you believe this document breaches copyrights.
We will remove access to the work immediately and investigate your claim.

1 **Origin of the synergistic effect between TiO₂ crystalline phases in the Ni/TiO₂-**
2 **catalyzed CO₂ methanation reaction**

3
4 *Davina Messou,^a Vincent Bernardin,^b Frédéric Meunier,^c Marta Borges Ordoño,^d Atsushi*
5 *Urakawa,^{d,e} Bruno F. Machado,^f Vincent Collière,^a Régis Philippe,^b Philippe Serp,^{*,a} and*
6 *Carole Le Berre^{*,a}*

7
8 *^a LCC-CNRS, INPT, 205 route de Narbonne, 31077 Toulouse Cedex 4, France*

9 *^b Catalysis Polymers Processes and Materials (CP2M), Université de Lyon, UMR 5128*
10 *CNRS, CPE Lyon, Université Claude Bernard Lyon 1, France*

11 *^c Univ. Lyon, Université Claude Bernard Lyon 1, CNRS, IRCELYON, 2 Av. Albert Einstein,*
12 *69626 Villeurbanne, France.*

13 *^d Institute of Chemical Research of Catalonia (ICIQ), Av. Paisos Catalans 16, 43007*
14 *Tarragona, Spain*

15 *^e Catalysis Engineering, Department of Chemical Engineering, Delft University of*
16 *Technology, Van der Maasweg 9, 2629 HZ Delft, The Netherlands*

17 *^f Laboratory of Separation and Reaction Engineering - Laboratory of Catalysis and Materials*
18 *(LSRE-LCM), Chemical Engineering Department, Faculty of Engineering, University of*
19 *Porto, Rua Dr. Roberto Frias s/n, 4200-465 Porto, Portugal*

1 **Abstract.** The catalytic performances of TiO₂-supported Ni catalysts for the methanation of
2 CO₂ have been investigated using different crystalline phases of TiO₂ (rutile and anatase). The
3 catalytic activity of Ni depends appreciably on the nature of the support. The rate for CO₂
4 hydrogenation decreases in the order of 10Ni/TiO₂-*rutile* >> 10Ni/TiO₂-*anatase*. The use of a
5 mixture of catalysts containing 70% 10Ni/TiO₂-*anatase* + 30% 10Ni/TiO₂-*rutile* allows for a
6 significant increase of the reaction rate related to 100% 10Ni/TiO₂-*rutile*. Importantly, it has been
7 demonstrated that the two catalysts do not need to be in direct contact for the synergetic effect
8 to occur. DRIFTS *operando* analysis during the methanation reaction shows that adsorbed CO
9 accumulates on Ni/TiO₂-*anatase* and not on Ni/TiO₂-*rutile*, and that the role of the Ni/TiO₂-*rutile* is
10 to assist the hydrogenation of this adsorbed CO on the Ni/TiO₂-*anatase*. Increased CO₂
11 methanation is also observed by adding Ni-free TiO₂-*anatase* to 10Ni/TiO₂-*rutile*, indicating that
12 CO_x hydrogenation can also occur on bare TiO₂-*anatase* if activated hydrogen can be supplied by
13 another source. H₂-TPD analyses and catalytic tests performed after dilution of the catalysts
14 have shown that hydrogen spillover (mediated by surface or gas-phase species) is at the origin
15 of the synergy observed between the two catalysts for the Sabatier reaction.

16

17 **Key words:** CO₂ methanation, nickel, titania, spillover, rutile, anatase

18

19 **1. Introduction**

20 The reduction of greenhouse gas emissions, and particularly those of CO₂, which is the main
21 contributor to global warming, is one of the major challenges of the beginning of this century.

22 In addition to reducing the emissions of this gas, two major strategies have been proposed to
23 reduce the amount of CO₂ present in the atmosphere: its capture and storage [1-3] and its
24 chemical transformation [4-6]. The chemical transformation of CO₂ is particularly promising

1 as increasing amounts of low-cost and relatively pure CO₂ are available from current plants [7].
2 In this context, CO₂ methanation (Sabatier reaction) is particularly attractive [8-11]. CO₂ can
3 be combined with hydrogen (produced by water electrolysis using renewable electricity) to
4 produce methane (power-to-gas), which can be directly injected into existing natural gas
5 pipelines [12-14]. Therefore, CO₂ methanation makes it possible to combine an environmental
6 benefit with an economic opportunity.

7 The Sabatier reaction is an exothermic reaction that has been studied using catalytic systems
8 based on Group VIII metals (Ru, Rh, Co, Ni) supported on various oxides (TiO₂, SiO₂, Al₂O₃,
9 CeO₂, ZrO₂) [9, 11]. Nickel remains the metal of choice, due to its selectivity, activity, low
10 price and abundance [15-18]. Haldor Topsøe uses Ni-based catalysts supported on alumina for
11 its own methanation processes (TREMP™ process) [19], and continuous efforts are pursued to
12 develop active, selective and stable Ni-based catalysts able to operate under mild reaction
13 conditions [18, 20-25].

14 The role of TiO₂ has been recognized in many reactions, as it enhances the catalytic activity
15 due to specific metal-support interactions [26, 27]. TiO₂ exists in three main crystalline forms,
16 *i.e.* anatase (TiO_{2-anatase}), rutile (TiO_{2-rutile}) and brookite. Each phase exhibits different physical
17 and chemical properties, such as thermal stability, density and band gap as well as surface
18 structure [27, 28]. Several works have been conducted to investigate the influence of the support
19 in methanation catalysts: TiO₂ vs Al₂O₃ or SiO₂ supports, but also TiO_{2-anatase} vs TiO_{2-rutile} vs
20 TiO_{2-P25} (a commercial mixture of rutile and anatase phases) [29-34]. On cobalt-based catalysts,
21 the activity of a Co/TiO_{2-rutile} catalyst is remarkably higher than that of Co/TiO_{2-anatase}; and while
22 CH₄ is selectively produced on Co/TiO_{2-rutile}, CO is the main product on Co/TiO_{2-anatase}. From
23 an *in situ* DRIFT study, it was proposed that the high activity of Co/TiO_{2-rutile} is related to the
24 formation of strongly adsorbed CO species on this catalyst [29]. On Ru/TiO₂ catalysts, Prairie
25 *et al.* have shown that: i) the high Ru dispersion is believed to contribute to the enhanced activity

1 for CO₂ methanation, and ii) a synergy exists for mixtures of Ru/TiO_{2-*anatase*} and Ru/TiO_{2-*rutile*}
2 [30]. From a FTIR study, these authors have evidenced that Ru/TiO_{2-*anatase*} is a better catalyst
3 for CO production, while Ru/TiO_{2-*rutile*} is more efficient in CO hydrogenation (the rate
4 determining step of methanation). The resulting ranking is as follows: Ru/TiO_{2-*P25*} > Ru/TiO₂
5 (mechanical mixture of anatase and rutile to simulate P25) > Ru/TiO_{2-*rutile*} >> Ru/TiO_{2-*anatase*}.
6 Continuing with ruthenium, Sassoie *et al.* have used different catalyst preparation methods,
7 using different TiO₂ crystalline phases and ratios [31, 32]. Phase mixing was also performed at
8 different stages of the catalyst preparation *i.e.*, before RuO₂ deposition, and before or after
9 calcination at 450 °C. These studies have shown that the interaction between the RuO₂ particles
10 and the anatase and rutile TiO₂ phases during the calcination step dictates the performance of
11 the Ru/TiO₂ methanation catalyst. The positive effect of support mixing, correlated with RuO₂
12 migration and stabilization from TiO_{2-*anatase*} over TiO_{2-*rutile*}, was noticed only in the case where
13 the mixing was done before the calcination step. Regarding nickel-based catalysts, Bao *et al.*
14 have shown that the TOF on Ni/TiO_{2-*rutile*} is almost two orders of magnitude higher than that on
15 Ni/TiO_{2-*anatase*} for CO₂ methanation, independently of Ni loading and particle size [33]. *In situ*
16 IR and temperature-programmed surface reaction experiments have revealed that TiO_{2-*rutile*}
17 significantly enhances the CO dissociation and hydrogenation ability of Ni. To the best of our
18 knowledge, a possible synergy between the anatase and rutile phase of TiO₂ for CO₂
19 methanation has not yet been demonstrated in the case of nickel, although high catalytic
20 activities have been reported for Ni/TiO_{2-*P25*} catalysts [20].

21 In this study, we have focused our attention on the interaction between nickel and TiO_{2-*rutile*} and
22 TiO_{2-*anatase*} phases by studying the performances of Ni catalysts supported on TiO_{2-*rutile*}, TiO_{2-*anatase*}
23 and TiO_{2-*P25*}. We confirmed the better performances of Ni/TiO_{2-*rutile*} compared to Ni/TiO_{2-*anatase*},
24 and revealed for the first time a synergy between the two phases in the Ni/TiO_{2-*P25*}
25 catalyst or in physical mixtures of Ni/TiO_{2-*rutile*} and Ni/TiO_{2-*anatase*}. Catalyst characterizations,

1 as well as catalytic experiments performed with pure catalysts in two separated and successive
2 fixed-beds, demonstrate that hydrogen spillover is at the origin of the synergistic effect, but also
3 of the different reactivity of Ni/TiO_{2-rutile} and Ni/TiO_{2-anatase} catalysts.

4

5 **2. Methods**

6 **Catalyst synthesis.** The commercial TiO₂ supports with different structures used are TiO_{2-rutile}
7 (99.5 %, Janssen Chimica), TiO_{2-anatase} (99.8 %, Aldrich) and TiO_{2-P25} (Safic-Alcan). In some
8 experiments, TiO_{2-rutile} and TiO_{2-anatase} were physically mixed in the corresponding proportions
9 to those of TiO_{2-P25}.

10 The Ni catalysts were prepared by using an impregnation method. Ni(NO₃)₂, 6H₂O (99.9%
11 Strem Chemical) was dissolved in water, where TiO₂ (rutile, anatase or P25) was then added.
12 The mixture was stirred during 4 h. The water was evaporated to obtain the catalyst, which was
13 dried at 120 °C overnight, and calcined under air at 500 °C during 6 h. The desired quantity of
14 Ni(NO₃)₂, 6H₂O to reach a 10 % w/w was used. According to Inductively Coupled Plasma
15 (ICP) analyses, the amount of nickel deposited on each support is similar. The as-prepared
16 catalysts were denoted as 10Ni/TiO_{2-rutile}, 10Ni/TiO_{2-anatase} or 10Ni/TiO_{2-P25} (with 10
17 representing the Ni percentage on the support).

18 **Catalyst characterization.** The structural and textural properties of the catalysts were evaluated
19 using different characterization techniques. The specific surface area, pore volume and pore
20 size distribution of the samples were obtained from the isothermal adsorption/desorption of
21 nitrogen at -196 °C on a Quantachrome autosorb instrument with N₂ automatic injection. The
22 specific surface area was determined from the linear part of the Brunauer-Emmett-Teller (BET)
23 plot. The pore volume was measured on the isotherm at P/P₀ = 0.97. The pore size distribution
24 was obtained by BJH treatment applied to the desorption branch of the isotherm. All samples

1 were pretreated under vacuum at 90 °C for 1 h to remove adsorbed water, then at 250 °C during
2 10 h for all other physisorbed species.

3 The amount of surface metal was quantified by chemisorption. Hydrogen was used to
4 determine the dispersion of the metal particles for each catalyst. In a first step, the sample (200
5 mg) was reduced using hydrogen (30 mL·min⁻¹) at 400 °C (10 °C·min⁻¹) during 4 h. Argon was
6 introduced at the same temperature for 2 h, and then maintained while the reactor cooled to
7 room temperature. At this stage of the analysis, pulses of H₂ were injected on the catalyst, and
8 the amount of residual gas was measured using a TCD detector (Quantachrome autosorb
9 instrument). The metallic dispersion D_{Ni}(%) of the catalysts was calculated from the amount of
10 irreversibly adsorbed hydrogen (HC): $D(\%) = HC/N_T * 100$ (N_T is the total quantity of metallic
11 atom in the sample).

12 Temperature-Programmed Reduction (TPR) experiments were performed with a
13 Micromeritics chemisorb 2700. Firstly, the catalyst (100 mg) was heated to 200 °C (10 °C·min⁻¹)
14 for 1 h. After the reactor cooled to room temperature, an argon flow (30 mL·min⁻¹) swept the
15 sample for 30 minutes. In a second step, the catalyst was reduced under a gaseous mixture of
16 10% H₂/Ar (30 mL·min⁻¹) with a heating ramp of 10 °C·min⁻¹ to 850 °C. The amount of
17 hydrogen consumed was monitored using a TCD. Peaks of hydrogen consumption were
18 obtained as a function of the temperature.

19 The distribution, shape, and size of the metal particles were obtained using a JEOL JEM
20 1011 transmission electron microscope (TEM). The average particle size was determined by
21 measuring at least 100 particles for each sample analyzed and using the following formula: Ni
22 particle size = $\sum n_i d_i^3 / \sum n_i d_i^2$ (d_i = diameter of n_i particles). The high-resolution analyses were
23 conducted on a JEOL JEM 2100F equipped with a field emission gun (FEG) operating at 200
24 kV with a point resolution of 2.3 Å and a JEOL JEM-ARM200F Cold FEG operating at 200
25 kV with a point resolution of > 1.9 Å. The crystalline structure of the samples was determined

1 on a D8 Advance Bruker Diffractometer (XRD) using Cu K α radiation ($\lambda = 0.15418$ nm) as X-
2 ray source. The surface of a sample, to a depth of 1 to 10 nm, was observed by X-ray
3 Photoelectron Spectroscopy (XPS) using a Thermo Scientific K-alpha spectrometer equipped
4 with an aluminum monochromatic source (Al K α , $h\nu = 1486.6$ eV). Data were processed using
5 the Thermo Advantage $\text{\textcircled{C}}$ software.

6 DRIFTS spectra were collected using a Harrick cell (powder, *ca.* 30 mg) fitted in a Nicolet
7 8700 FT-IR (MCT detector). Gas-phase CH $_4$ and CO $_2$ were quantified after the DRIFTS using
8 a quartz 10-cm pathlength IR gas-cell fitted in a Bruker FT-IR. The CO signal was very low
9 (and not visible for Ni/Rutile) and was not quantified. The band area of adsorbed CO was
10 calculated and compared for three catalysts. The DRIFTS analysis provides quantitative
11 comparison within 10% as long as evolution of the same sample (or same mixture of samples)
12 are compared with each other (hence in each case the optical pathway remains the same). In our
13 case, it is also coherent to compare mechanical mixtures of similar materials, since scattering
14 and absorption coefficient should be similar.

15 In order to understand the behavior and the synergetic effect between the anatase and rutile
16 phases, space-resolved gas sampling was performed using a fused silica capillary (I.D. = 150
17 μm) inserted in the catalyst bed that moved along the axial direction; data was collected for
18 each position (9 positions in total) along the catalyst using a mass spectrometer (OmniStar,
19 Pfeiffer Vacuum). The custom-built reactor was made of 1/4" quartz tube with an I.D. of 4 mm.
20 For each experiment, 100 mg of catalyst was used with a particle size between 125 and 200 μm .

21 H $_2$ -TPD-MS (Altamira Instruments AMI-300 device) was used to elucidate the nature of the
22 hydrogen adsorbed species during the desorption step. First, the catalyst (or support) (100 mg)
23 was purged with helium at 120 $^{\circ}\text{C}$ for 1 h in order to clean the surface of the sample. The sample
24 was then reduced *in situ* at 400 $^{\circ}\text{C}$ (10 $^{\circ}\text{C}\cdot\text{min}^{-1}$) for 4 h using a 1/4 mixture of He/H $_2$ and then

1 cooled to room temperature under the same atmosphere. The sample was then swept with
2 helium at a flow rate of 30 mL·min⁻¹ for 1 h to remove physisorbed and/or weakly bound
3 species. TPD was performed by heating the sample from 50 to 700 °C with a heating ramp of
4 10 °C·min⁻¹ in helium and the TPD spectra were recorded.

5 **Catalytic tests.** The catalytic tests for the methanation of CO₂ were performed using a
6 continuous-flow stainless steel fixed bed reactor (height = 300 mm, *e.d.* = 9.52 mm, *i.d.* = 7.9
7 mm) under a total pressure of 6.1 bar. 200 mg of catalyst with a particle size in the 100-200 μm
8 range were mixed with 1800 mg of SiC (Alfa Aesar). Before the catalytic test, the catalyst was
9 reduced *in situ* at 400 °C for 4 h under a 1/4 mixture of N₂/H₂, at atmospheric pressure. Then,
10 experiments were performed at a constant WHSV (Weigh Hourly Space Velocity) of 2750
11 NmL_{CO₂}·h⁻¹·g⁻¹. under a N₂/H₂/CO₂ gas mixture of 1/4/1 at 340 °C and 6.1 bar. Some tests were
12 also conducted at 260 °C and 6.1 bar, or at 340 °C and 1 bar. Some tests were also performed
13 by dilution of the catalyst in TiO₂ support instead of pure SiC. In typical dilution tests, 200 mg
14 of catalyst were diluted in 1000 mg of TiO₂ support and 800 mg of SiC.

15 The composition of the reactant/product mixture was analyzed using an on-line gas
16 chromatograph (500 Clarius) equipped with two TCD: one with argon as gas vector to quantify
17 H₂, CH₄, and CO, and another with helium to quantify CO₂. The GC is equipped with two
18 Shincarbon columns (1/8, 2.0 mm, 80/100), and recorded the formation of methane and
19 conversion of H₂ and CO₂ every 8 min.

20 The different response coefficients determined from the GC calibration allowed us to calculate
21 the molar fractions (X) of the different molecules considered during the methanation reaction,
22 as follows:

23
$$X_a = \left(\frac{\text{Area of a signal}}{\text{Area of N}_2 \text{ signal}} \right) \times \frac{1}{k_a}$$

24

1 With a = CO₂, CH₄, H₂, CO and k = response coefficient.

2 The conversion rates of the reagents were then calculated as follows:

3
$$CO_2 \text{ conversion} = \left(1 - \frac{X_{CO_2}}{X_{CO_2} + X_{CH_4} + X_{CO}}\right) \quad H_2 \text{ conversion} = \left(1 - \frac{H_2 \text{ outlet flow}}{H_2 \text{ inlet flow}}\right)$$

4 With $H_2 \text{ outlet flow} = \text{Dry flow outlet} \times X_{H_2}$

5 With Dry Flow, the gas flow without water formed during the reaction.

6
$$\text{Dry flow outlet} = \left(\frac{CO_2 \text{ inlet flow}}{X_{CO_2} + X_{CH_4} + X_{CO}}\right) \quad CH_4 \text{ yield} = \left(\frac{CH_4 \text{ outlet flow}}{CO_2 \text{ inlet flow}}\right)$$

7 With $CH_4 \text{ outlet flow} = \text{Dry flow outlet} \times X_{CH_4}$

8 $CO \text{ yield} = CO_2 \text{ conversion} - CH_4 \text{ yield}$

9
$$CH_4 \text{ selectivity} = \left(\frac{\%CH_4 \text{ yield}}{\%CO_2 \text{ conversion}}\right) \quad CO \text{ selectivity} = \left(\frac{CO \text{ yield}}{CO_2 \text{ conversion}}\right)$$

10

11 Possible thermodynamic, heat transfers and mass transfer limitations have been checked (see
12 SI 1 and SI 2). When not specified, all the results are due to an intrinsic kinetic effect and thus
13 reflect a catalytic effect. In order to remove any effect of a different level of conversion between
14 experiments, the quantitative comparison of catalysts has been achieved through a robust
15 kinetic comparison on the basis of estimated inlet CO₂ consumption rates ($r_{CO_2}^i$) at the reactor
16 inlet. This goal was achieved thanks to a non-isothermal and non-isobaric unidimensional
17 pseudo-homogeneous plug-flow reactor model combined with the regression of a limited set of
18 kinetic parameters of the kinetic model from Champon *et al.*[36] More details on this approach
19 are available in the SI 3. The CO₂ consumption rates at the inlet ($r_{CO_2}^i$), can then be used to
20 calculate corresponding TOF_i at the reactor inlet. These TOF_i, which refer to the number of
21 reacted molecules per surface active Ni per unit of time at the reactor inlet, have been calculated

1 considering dispersion data (TEM mean particle size after testing) obtained from a universal
2 mathematical relation [35].

3 Catalyst stability was evaluated considering a deactivation parameter (DP) based on the
4 evolution of the inlet reaction rate of CO₂ hydrogenation with time on stream (TOS) defined as
5 follows:

$$6 \quad DP = \frac{(r_{CO_2}^i)_{TOS=20h} - (r_{CO_2}^i)_{TOS=1h}}{(r_{CO_2}^i)_{TOS=1h}}$$

7 Because of possible differences in catalyst activity and active specie dispersion, a Turn Over
8 Number (TON, expressed in mol_{CO₂} converted per mol_{Ni surf.}) is always given simultaneously to
9 reflect the corresponding work of the catalyst.

10

11

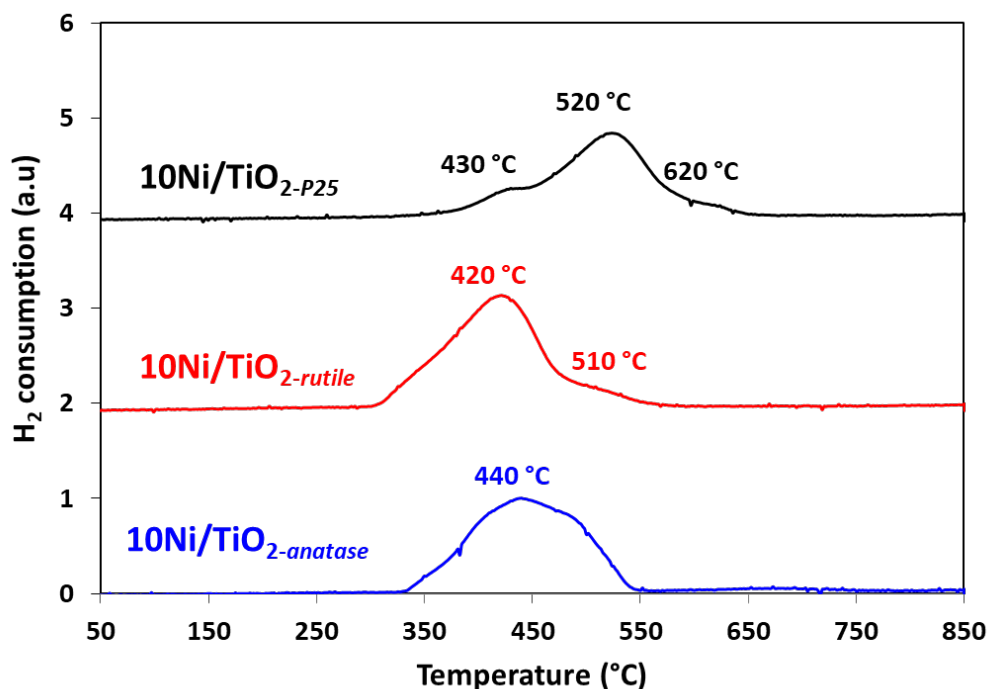
12 **3. Results**

13 ***3.1. Catalyst characterization***

14 The specific surface area, pore volume, average pore diameter, Ni loading (ICP), Ni mean
15 particle size and dispersion of the investigated samples are shown in Table 1. The BET area of
16 commercial TiO₂ supports follows the sequence TiO_{2-P25} (57 m² g⁻¹) > TiO_{2-anatase} (10 m² g⁻¹) >
17 TiO_{2-rutile} (4 m² g⁻¹). As already reported for similar catalysts [20], the addition of nickel by
18 impregnation induces a decrease of the specific surface area for the TiO_{2-P25}-based catalyst.
19 Figure 1 shows the H₂-TPR profiles of the calcined Ni/TiO₂ samples, which correspond to the
20 reduction of NiO. The catalysts can be classified according to their reducibility in the following
21 order: 10Ni/TiO_{2-rutile} ~ 10Ni/TiO_{2-anatase} > 10Ni/TiO_{2-P25}. For 10Ni/TiO_{2-rutile} and 10Ni/TiO₂₋
22 *anatase* catalysts, the H₂-TPR profile presents a main reduction peak at 420 and 440 °C,

1 respectively. An easier reduction of NiO to Ni⁰ for Ni/TiO_{2-rutile} compared to Ni/TiO_{2-anatase} has
2 been previously reported [37]. The 10Ni/TiO_{2-P25} catalyst profile is relatively broad (stepwise
3 Ni reduction) and the lower reducibility suggests a stronger interaction between Ni and the
4 support, arising presumably from a smaller Ni particle size. Previous H₂-TPR experiments on
5 Ni/TiO_{2-anatase} and Ni/TiO_{2-rutile} have also proposed a stepwise reduction of Ni [33]. Finally, if
6 the discussion on the TPR profiles of Ni/TiO₂ catalysts are generally limited to the reduction of
7 NiO species presenting different type of interaction with the support, some works [38, 39] also
8 reported that the NiO phase reduction can be accompanied by a partial reduction of Ti⁴⁺ to Ti³⁺,
9 resulting in the formation of O_v- Ti³⁺ site (where O_v denotes oxygen vacancy). It is not possible
10 to exclude the occurrence of such a phenomenon in our case.
11 The Ni particle size was obtained from both XRD and TEM analyses (Table 1). The TEM and
12 XRD analyses confirmed a smaller Ni particle size on the TiO_{2-P25} support.

13



14

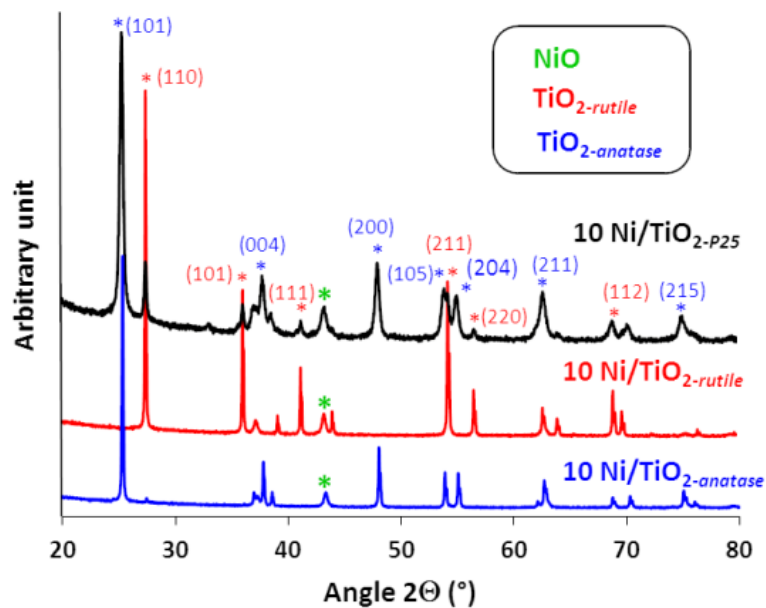
15 **Figure 1.** H₂-TPR profiles for the 10Ni/TiO_{2-anatase}, 10Ni/TiO_{2-rutile} and 10Ni/TiO_{2-P25} catalysts.

16

1 In XRD, the characteristic NiO peak is identified at $2\theta = 43.55^\circ$ (Figure 2). Although it has
 2 been shown that the anatase-rutile transformation of the TiO_2 support is facilitated by the
 3 metallic ions formed during the reduction [40]; such phenomenon was not significant in the
 4 present study. The amount of anatase phase in $\text{TiO}_2\text{-P25}$ (78 %) was determined from the
 5 equation proposed by Spurr and Myer [41]:

$$6 \quad \% \text{ anatase} = \left(1 + 1.26 * \left(\frac{I_r}{I_a}\right)\right)^{-1}$$

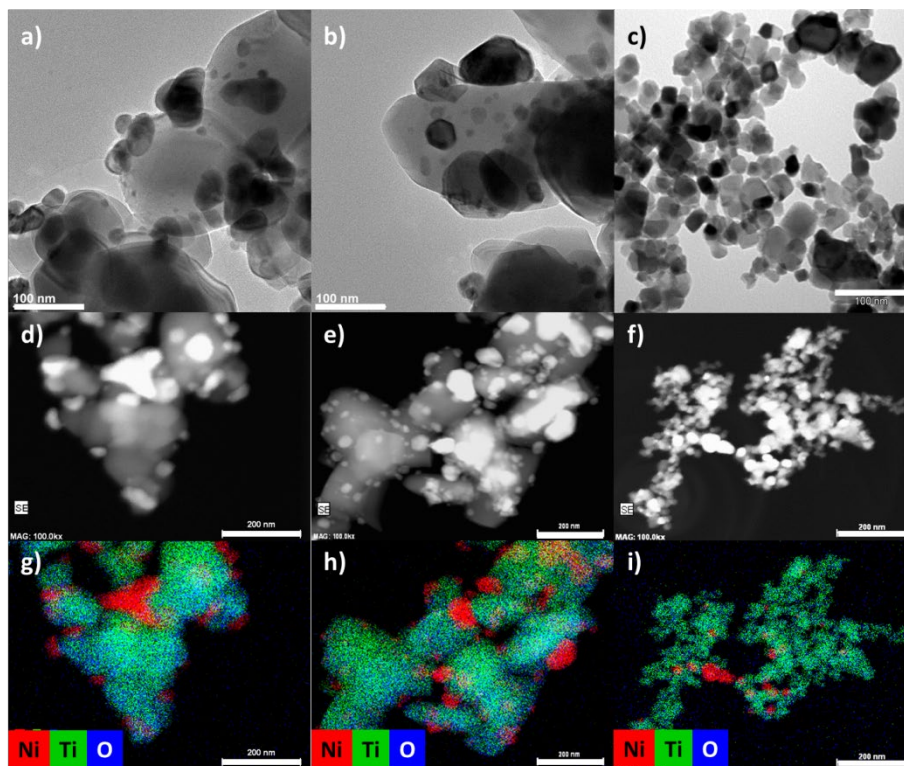
7 where I_a ($2\theta = 25.4^\circ$) and I_r ($2\theta = 27.6^\circ$) are the XRD peak intensities of the anatase and rutile
 8 crystal components, respectively.



9
 10 **Figure 2.** XRD diffractograms for the 10Ni/TiO₂-anatase, 10Ni/TiO₂-rutile and 10Ni/TiO₂-P25
 11 catalysts.

12
 13 The images obtained by conventional TEM (Figure 3a-c) allowed us to compare the
 14 morphology of the catalysts and to determine the corresponding Ni particle size distribution

1 (Figure S1). STEM-HAADF images (Figure 3d-f) and EDX mapping (Figure 3g-i) demonstrate
2 the presence of Ni particles on the three catalysts. The Ni particles are larger on $\text{TiO}_2\text{-rutile}$ and
3 $\text{TiO}_2\text{-anatase}$ supports. Nickel is relatively well dispersed, especially on the 10Ni/ $\text{TiO}_2\text{-P25}$
4 catalyst, presumably due to the significantly higher surface area of this support. Although TEM
5 studies have revealed that Ni particles show a non-wetting morphology when grown on $\text{TiO}_2\text{-}$
6 *anatase* and a wetting morphology when grown on the rutile (101) surface [42], in our case
7 HRTEM observations (Figure S2) were not conclusive regarding such a phenomenon, even if
8 it appears that the Ni particles on $\text{TiO}_2\text{-rutile}$ were more faceted than the ones on $\text{TiO}_2\text{-anatase}$
9 (Figures 3a,b and Figure S3).



10
11 **Figure 3.** TEM images of a) 10Ni/ $\text{TiO}_2\text{-anatase}$, b) 10Ni/ $\text{TiO}_2\text{-rutile}$ and c) 10Ni/ $\text{TiO}_2\text{-P25}$; STEM-
12 HAADF images of d) 10Ni/ $\text{TiO}_2\text{-anatase}$, e) 10Ni/ $\text{TiO}_2\text{-rutile}$ and f) 10Ni/ $\text{TiO}_2\text{-P25}$; and EDX
13 mapping of g) 10Ni/ $\text{TiO}_2\text{-anatase}$, h) 10Ni/ $\text{TiO}_2\text{-rutile}$ and i) 10Ni/ $\text{TiO}_2\text{-P25}$. Scale bar (a-c): 100nm;
14 (d-i): 200 nm.

15

1 The dispersion values of the catalysts obtained by hydrogen chemisorption are very low (0.1-
2 1%). Similar results have already been reported, and have been rationalized by the fact that
3 hydrogen adsorption on Ni/TiO₂ is an activated process [43]. In all cases, the dispersion values
4 calculated from the average particle sizes determined by TEM differ from the chemisorption
5 experimental values. However, the trends remain the same. The H₂ adsorption capacity on the
6 various catalysts decreases according to the following order: TiO_{2-P25} > TiO_{2-rutile} ≈ TiO_{2-anatase}.
7 Since CO adsorption at low temperature (< 200 °C) may result in [Ni(CO)₄] formation [44], Ni
8 corrosion and Ni deposition in the setup and lines, CO chemisorption was not performed.
9 XPS analyses were performed just after reducing the samples at 400 °C. The deconvolutions of
10 the Ni 2p_{3/2} region of the three catalysts are presented on Figure 4. The chemical states of Ni
11 considered are the following [45-48]:

- 12 - Ni⁰ particles: 1 peak at 852.6 eV and 2 satellite peaks (856.3 eV and 858.7 eV)
- 13 - NiO: 1 peak at 853.7 eV and 4 satellite peaks (855.4 eV, 860.9 eV, 864.0 eV, and
14 866.3 eV)
- 15 - Ni(OH)₂: 1 peak at 855.6 eV and 5 satellite peaks (855.7 eV, 857.7 eV, 860.5 eV,
16 861.5 eV and 866.5 eV).

17 Nickel is present as Ni⁰, NiO and Ni(OH)₂ on the three catalysts. The superposition of the bands
18 does not show any significant differences between the different catalysts at the level of the
19 binding energies. Table 2 groups relevant results obtained after deconvolution of the XPS
20 spectra. The atomic percentage and binding energies associated with all the corresponding
21 peaks are given in Table S8. The relative atomic percentage of Ni⁰ follows the order 10Ni/TiO₂₋
22 *anatase* > 10Ni/TiO_{2-rutile} > 10Ni/TiO_{2-P25}. The lower amount of Ni⁰ on 10Ni/TiO_{2-P25} is in
23 accordance with the TPR results, and should be due to the smaller particle size measured for
24 this catalyst. Indeed, small Ni⁰ particles interact strongly with the support, and react with
25 oxygen at a faster rate than with large particles [49].

Table 1. Specific surface area, pore volume, average pore diameter, Ni loading (ICP), Ni mean particle size and dispersion of the investigated samples.

Sample	BET surface area (m ² g ⁻¹)	Pore volume (cm ³ g ⁻¹)	Average pore diameter (nm)	%Ni	Ni particle size (nm) ^a	Ni particle size (nm) ^b	Ni particle size (nm) ^c	D _{Ni} (%) ^d
TiO ₂ - <i>anatase</i>	10	0.12	15	-	-	-	-	-
TiO ₂ - <i>rutile</i>	4	0.05	15	-	-	-	-	-
TiO ₂ - <i>P25</i>	57	0.31	17	-	-	-	-	-
10Ni/TiO ₂ - <i>anatase</i>	10	0.14	17	11.0	31	24	27	4.4
10Ni/TiO ₂ - <i>rutile</i>	4	0.05	16	10.1	33	27	29	4.1
10Ni/TiO ₂ - <i>P25</i>	47	0.37	15	10.1	22	17	20	6.1

^a The Ni crystal size after reduction, from TEM.

^b The Ni crystal size after reduction, from XRD.

^c The Ni crystal size after catalysis (340°C, time-on-stream (TOS) = 25 h), from TEM.

^d Dispersion of Ni, calculated from the average particle sizes determined by TEM.

Regarding the difference between 10Ni/TiO_{2-*anatase*} (36 % Ni⁰) and 10Ni/TiO_{2-*rutile*} (25.5 % Ni⁰), it might be related to the different Ni/Ti surface atomic ratios in these samples. The 10Ni/TiO_{2-*rutile*} catalyst shows a significantly higher ratio (0.81) than 10Ni/TiO_{2-*anatase*} (0.31), which should result from the lower surface area of the TiO_{2-*rutile*} support. Another explanation for the higher Ni/Ti surface atomic ratio observed on 10Ni/TiO_{2-*rutile*} could arise from the fact that Ni particles on TiO_{2-*anatase*} are wrapped by a thin TiO_x overlayer [33, 50].

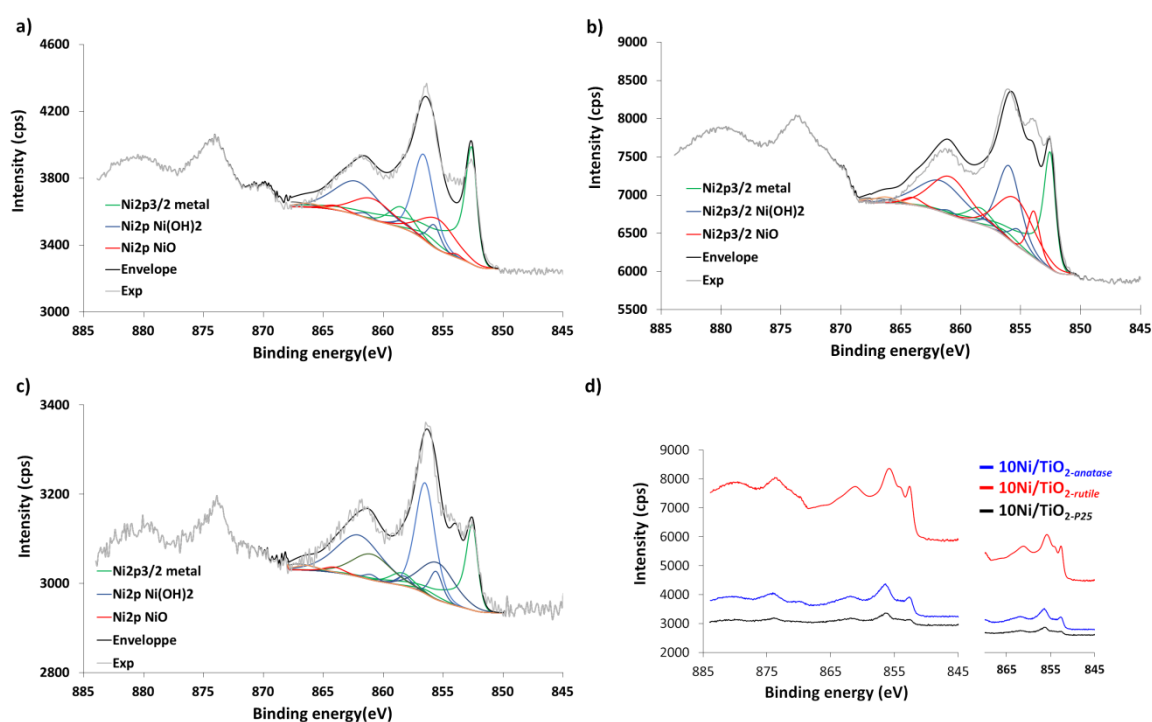


Figure 4. Deconvolutions of Ni 2p_{3/2} peak of the catalysts, after *ex-situ* reduction under H₂ at 500 °C a) 10Ni/TiO_{2-*anatase*}, b) 10Ni/TiO_{2-*rutile*}, and c) 10Ni/TiO_{2-*P25*}. d) Superposition of the Ni 2p_{3/2} bands of the three samples.

However, our HRTEM observations and STEM-EDX analyses (Figures S4), as well as the catalytic results (see below) do not support this possibility on any of the three supports. This is understandable if we consider that for Ni/TiO₂ catalysts, strong metal support interactions are

significant when a high calcination temperature is used, typically around 800 °C [51, 52]. The low Ni/Ti surface atomic ratio measured for 10Ni/TiO_{2-P25} should be related to the much higher specific surface area of this catalyst. No significant changes in the Ni⁰ binding energy were noticed for the three catalysts, precluding significant differences in charge transfer between these samples, which could affect selectivity in the Sabatier reaction [53, 54]. This is expected if we consider the large Ni particle size; but we cannot exclude that some differences exist in the interfacial region between the metal and the support. Titanium is in the Ti⁴⁺ form, and the Ti³⁺ form characteristic of reduced TiO₂ [55] was not detected (Figure S5) under these conditions. From HRTEM observations, STEM-EDX analyses (Figures S4) and these XPS data, we can thus exclude the mobility of TiO_{2-x} over the nickel surface.

Table 2. Atomic relative percentage of Ni species, Ni⁰ and Ti binding energy and Ni/Ti at. ratios of the catalysts determined by XPS analyses after *ex situ* reduction under H₂ at 400 °C.

Catalyst	Ni ⁰ (%)	Ni(OH) ₂ (%)	NiO (%)	Ni ⁰ B.E. (eV)	Ti B.E. (eV)	Ni/Ti
10Ni/TiO _{2-anatase}	36.0	42.0	22.0	852.6	459.1	0.31
10Ni/TiO _{2-rutile}	25.5	35.6	38.9	852.5	459.2	0.81
10Ni/TiO _{2-P25}	19.7	50.6	29.6	852.6	459.3	0.14

Based on the above analyses, we can conclude that the main difference between the three catalysts arise mainly from the higher BET surface area of TiO_{2-P25}, which allows a better nickel dispersion on that support. The smaller Ni particles present on TiO_{2-P25} are more difficult to reduce than those supported on TiO_{2-anatase} or TiO_{2-rutile}. The higher dispersion of Ni on 10Ni/TiO_{2-P25} should result in a higher catalytic activity for CO₂ methanation, as demonstrated by Wei *et al.* [20].

3.2. Evaluation of the catalytic behavior

The catalytic performances of the obtained Ni/TiO₂ catalysts towards the reaction of CO₂ methanation were studied under different configurations: i) pure catalysts in single fixed-bed reactor configuration; ii) mixture of catalysts in single fixed-bed reactor configuration, and iii) pure catalysts in two separated and successive fixed-beds. Reproducibility tests were regularly performed on the 10Ni/TiO_{2-P25} catalyst, showing experiment error in the range $\pm 5\%$.

Pure catalysts in single fixed-bed reactor configuration. Figure 5 shows the CO₂ consumption rates at the inlet of the reactor ($r_{\text{CO}_2}^i$) and CH₄ selectivity of 10Ni/TiO_{2-*anatase*}, 10Ni/TiO_{2-P25}, and 10Ni/TiO_{2-*rutile*} at 260 °C. Table 3 summarizes the values of CO₂ conversion, CH₄ selectivity, CO₂ consumption rate and initial TOF at 260 and 340 °C. At 260 °C, the conversion values were all below 10%, far from the thermodynamic equilibrium composition. Thus, any thermodynamic limitation can be excluded at 260°C (see SI 1-2 for further details). The reaction rate at the inlet of the reactor $r_{\text{CO}_2}^i$ of the three catalysts follows the order: 10Ni/TiO_{2-P25} > 10Ni/TiO_{2-*rutile*} >> 10Ni/TiO_{2-*anatase*} ($k_{\text{CO}_2\text{meth}}$ kinetics constants are given in SI.2, Table S7). These results confirm the findings of Bao *et al.* for Ni/TiO₂ catalysts; *i.e.* Ni/TiO_{2-*rutile*} is much more active than Ni/TiO_{2-*anatase*} for CO₂ methanation [33]. Since the 10Ni/TiO_{2-P25} catalyst presents a smaller mean Ni particle size compared to 10Ni/TiO_{2-*rutile*} and 10Ni/TiO_{2-*anatase*} catalysts (Table 1), the TOF_i led to the following order 10Ni/TiO_{2-*rutile*} \approx 10Ni/TiO_{2-P25} >> 10Ni/TiO_{2-*anatase*}. Additionally, as the Ni particle size is significantly smaller on TiO_{2-P25} than on TiO_{2-*rutile*}, no obvious structure sensitivity is apparent in the particle size range investigated. Considering that: i) the Ni particle size is similar on 10Ni/TiO_{2-*anatase*} and 10Ni/TiO_{2-*rutile*} catalysts, ii) no TiO_x overlayer is present on these particles, and iii) the nature of the metal/support interaction is not significantly different for these catalysts (except maybe at the interface), it is reasonable to propose that all catalysts should contain mainly interfacial active sites, *i.e.* those located at the gas/particle/support interface [56].

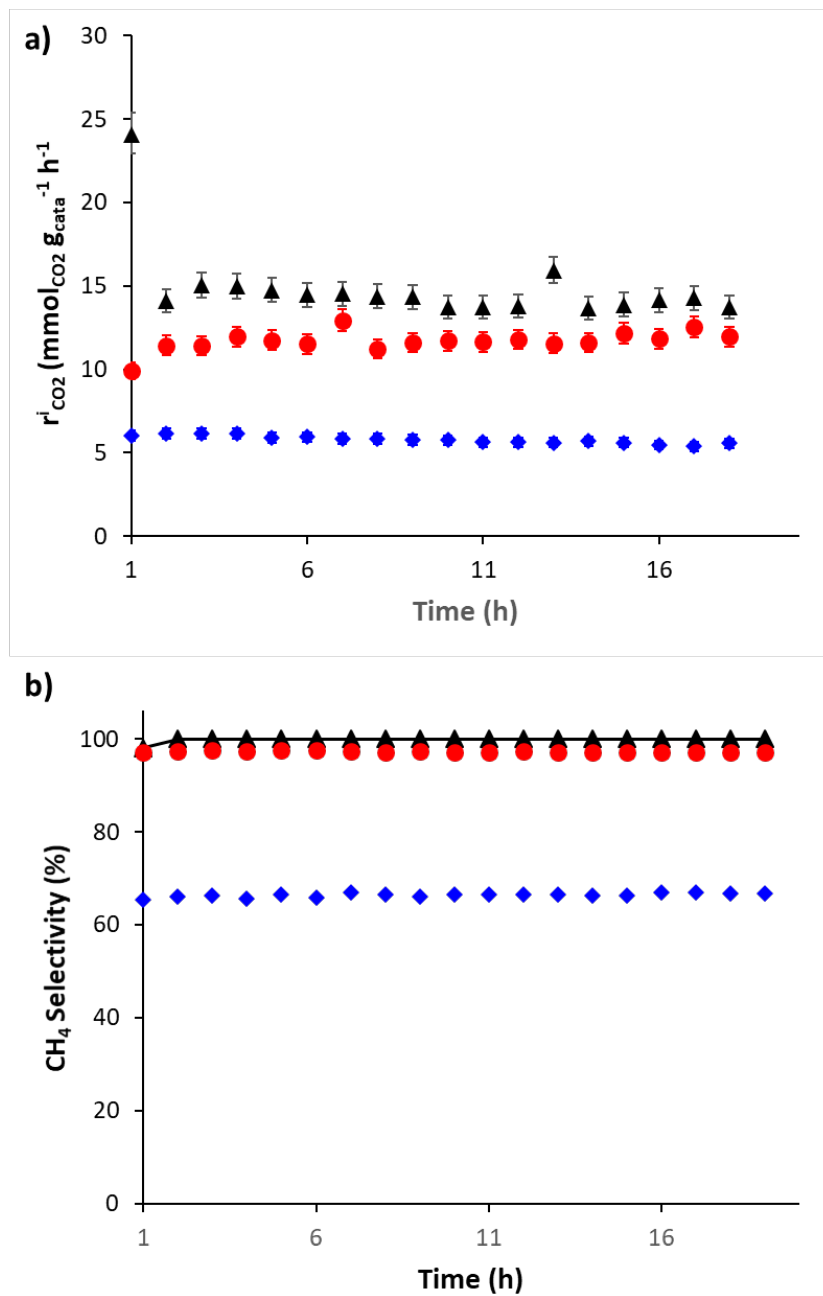


Figure 5. Comparison of: a) CO₂ consumption rates at the inlet of the reactor; and b) CH₄ selectivity of 10Ni catalyst on 10Ni/TiO₂-*anatase* (blue diamonds), 10Ni/TiO₂-*rutile* (red circles) and 10Ni/TiO₂-*P25* (black triangles) at 260 °C.

Table 3. CO₂ conversion, CH₄ selectivity, CO₂ consumption rate and initial TOF (TOF_i) of Ni catalysts on different supports obtained at 260 °C and 340 °C.

Catalyst	CO ₂ conv. (%) ^a	CH ₄ selec.(%) ^a	$r_{\text{CO}_2}^i$ (mmolCO ₂ g _{cat} ⁻¹ h ⁻¹)	TOF _i (h ⁻¹)
10Ni/TiO ₂ - <i>anatase</i>	4.5 (42.6)	66.4 (79)	5.8	71
10Ni/TiO ₂ - <i>rutile</i>	8.8 (78.4)	99.5 (98.3)	11.7	166
10Ni/TiO ₂ - <i>P25</i>	11.0 (95.6)	99.9 (99.5)	15.1	146

^a The values between brackets are the value obtained at 340 °C.

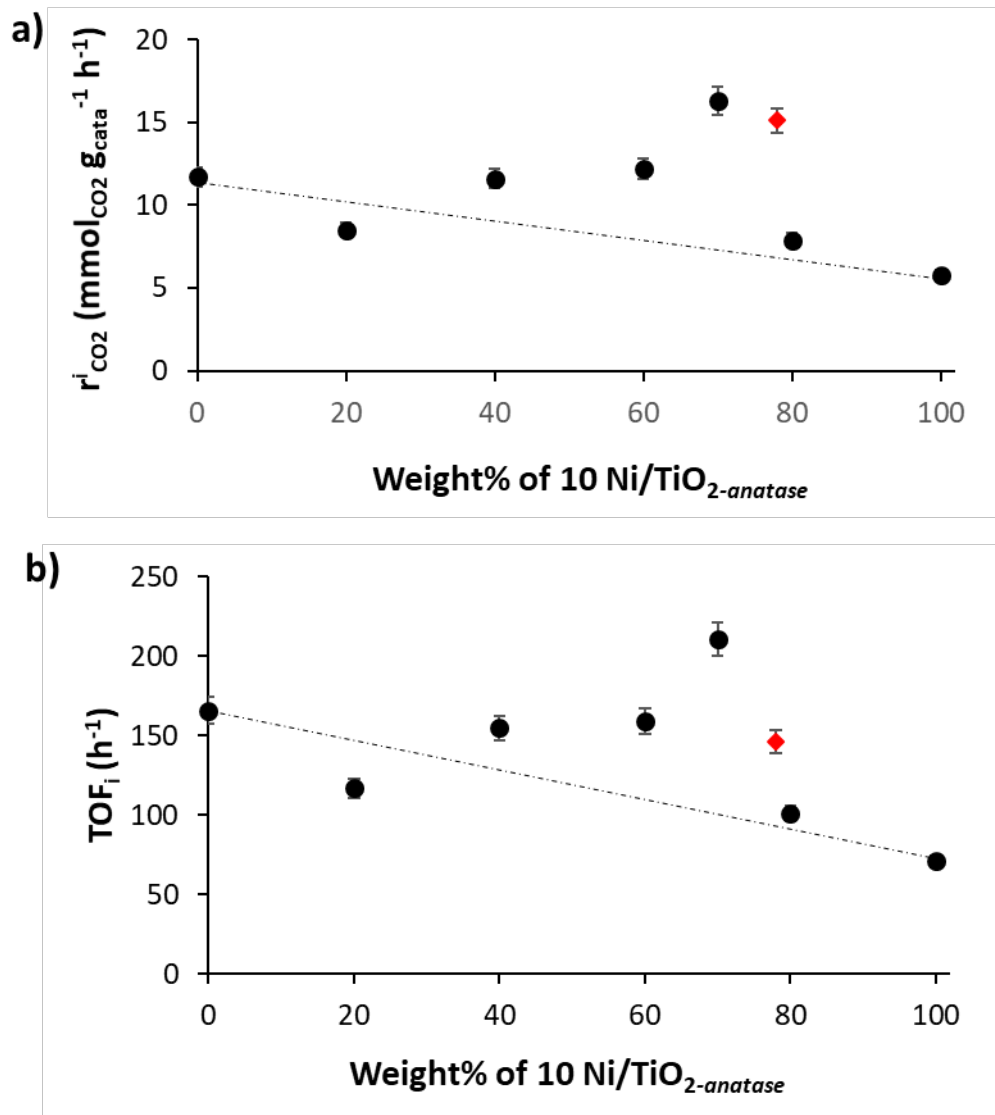
1 As far as selectivity is concerned, it follows the order: $10\text{Ni}/\text{TiO}_2\text{-}P25 \approx 10\text{Ni}/\text{TiO}_2\text{-}rutile >$
2 $10\text{Ni}/\text{TiO}_2\text{-}anatase$. In the case of $10\text{Ni}/\text{TiO}_2\text{-}anatase$, higher amounts of CO are produced. It has
3 also been shown that the binding strengths of key reaction intermediates at the metal/oxide
4 interface determine the reaction pathways and selectivity in CO₂ hydrogenation reactions [57,
5 58]. The presence of Ni single atoms or very small nanoparticles or clusters that bind CO too
6 weakly, could also facilitate an easy desorption [54, 59, 60].

7 The stability of the catalyst is also an important property for CO₂ methanation because of
8 possible Ni sintering and coke deposition under the exothermic reaction conditions, which can
9 lead to fast deactivation. The catalyst stability was investigated for the three catalysts using
10 deactivation parameter (DP) representing the relative loss in reaction rate at the inlet of the
11 reactor and a corresponding TON. These evaluations were done at 260 °C and 340 °C under a
12 constant GHSV of 16500 NmL/h/g_{cata} for a time on stream of 20 h. For the experiments at 260
13 °C (Figure S6), no detectable deactivation occurs during 20 h for $10\text{Ni}/\text{TiO}_2\text{-}rutile$ and $10\text{Ni}/\text{TiO}_2\text{-}$
14 $P25$ and a slight one for $10\text{Ni}/\text{TiO}_2\text{-}anatase$ with a DP around 7 %. Final TON values of 1340, 2750
15 and 2214 are reached for a TOS of 20 h at 260 °C for $10\text{Ni}/\text{TiO}_2\text{-}anatase$, $10\text{Ni}/\text{TiO}_2\text{-}rutile$ and
16 $10\text{Ni}/\text{TiO}_2\text{-}P25$ respectively. The same experiments run at 340°C (Figure S6) indicate again that
17 no detectable deactivation was observed for $10\text{Ni}/\text{TiO}_2\text{-}rutile$ and $10\text{Ni}/\text{TiO}_2\text{-}P25$ and a pronounced
18 one is observed for $10\text{Ni}/\text{anatase}$ (DP = -62%). Nonetheless, the high conversion level
19 encountered with $10\text{Ni}/\text{TiO}_2\text{-}P25$ at this temperature is too close to the thermodynamic
20 equilibrium to draw any robust conclusion on the catalyst stability at this temperature for this
21 catalyst. One can just reasonably expect that it is due to its similarity with the rutile catalyst.

22 The final TON values reached during these experiments are logically higher than the former
23 ones and are of 12 710, 27 250 and 22 370 for $10\text{Ni}/\text{TiO}_2\text{-}anatase$, $10\text{Ni}/\text{TiO}_2\text{-}rutile$ and $10\text{Ni}/\text{TiO}_2\text{-}$
24 $P25$ respectively. Deactivation of Ni/TiO₂ catalysts during CO₂ methanation has been ascribed
25 either to coke formation through either CH₄ decomposition, or *via* CO disproportionation [24],

1 or to nickel oxidation [61]. It is interesting to notice that this deactivation is more likely on the
2 catalyst prepared on the anatase phase, which also produces more CO available for
3 disproportionation.

4 ***Mixtures of catalysts in single fixed-bed reactor configuration.*** In order to obtain more
5 information on the influence of the TiO₂ phase on the catalytic performances, calcined
6 10Ni/TiO_{2-anatase} and 10Ni/TiO_{2-rutile} catalysts were physically mixed at different weight ratio.
7 Table 4 shows the CO₂ conversion, CH₄ selectivity, CO₂ consumption rate and inlet TOF_i of
8 these catalyst mixtures. Figure S7 shows the evolution with ToS of CO₂ consumption rate and
9 CH₄ selectivity. The use of 10Ni/TiO_{2-anatase} and 10Ni/TiO_{2-rutile} catalyst mixtures (presenting
10 similar particle sizes) improves the CO₂ consumption rate, and a synergistic effect is evidenced
11 ($k_{\text{CO}_2\text{meth}}$ kinetics constants are given in SI.2, Table S7). Interestingly, the synergistic effect was
12 noticed even if the catalysts were mixed after the calcination step, which differs from the work
13 of Sassoie *et al.* [31,32]. Figure 6 shows the inlet CO₂ consumption rate and the corresponding
14 TOF_i for the mixed series from pure 10Ni/TiO_{2-anatase} to pure 10Ni/TiO_{2-rutile} catalyst, as a
15 function of the anatase content in the supports. A synergy is clearly observed for a % of
16 10Ni/TiO_{2-anatase} between 40 and 80%, as the catalyst mixtures are more active than the
17 corresponding calculated weighted rates based on single-phase rates. The highest TOF_i was
18 obtained for a ratio 70/30, close to the 72/28 ratio of TiO_{2-P25}. It is worth noting that the TOF_i
19 of the 70/30 mixture (211 h⁻¹, Table 4) is markedly higher than that of 10Ni/TiO_{2-P25} (146 h⁻¹).



1

2 **Figure 6.** a) CO₂ consumption rate at the inlet of the reactor; and b) TOF_i at 260 °C for the
 3 mixed series from pure 10Ni/TiO_{2-*anatase*} to pure 10Ni/TiO_{2-*rutile*} catalyst, as a function of the
 4 anatase content. The full lines indicate the calculated weighted average of 10Ni/TiO_{2-*anatase*} and
 5 10Ni/TiO_{2-*rutile*} individual performances. The red diamond corresponds to the 10Ni/TiO_{2-*P25*}
 6 catalyst.

7

Table 4. CO₂ conversion, CH₄ selectivity, CO₂ consumption rate (sum of methanation reaction rate and RWGS reaction rate) at the inlet of the reactor, initial TOF, and specific activity of 10Ni/TiO_{2-*anatase*} + 10Ni/TiO_{2-*rutile*} at different ratio and 260 °C (average values after 20 h).

10Ni/TiO_{2-<i>anatase</i>}/10Ni/TiO_{2-<i>rutile</i>} (weight %)	CO₂ conv. (%)	CH₄ selec. (%)	r_{CO₂}ⁱ (mmol_{CO₂} g_{cat}⁻¹ h⁻¹)	TOF_i (h⁻¹)
100/0	4.5	66.4	5.8	71
80/20	6.1	87.9	7.9	101
70/30	11.9	97.8	16.3	211
60/40	9.1	92.7	12.2	159
40/60	8.7	94.7	11.6	155
20/80	6.5	94.7	8.5	117
0/100	8.8	97.2	11.7	166

1 **Pure catalysts in two separated and successive fixed-beds.** We performed a series of
 2 experiments with two successive beds of 10Ni/TiO_{2-*anatase*} and 10Ni/TiO_{2-*rutile*} (Figure S8 shows
 3 the two reactor configurations with the two separated beds). In the first configuration (**C1**), the
 4 gas flow passes first through a bed of 10Ni/TiO_{2-*rutile*}, and then through a separate bed of
 5 10Ni/TiO_{2-*anatase*}. In the second configuration (**C2**), the gas flow passes first through a bed of
 6 10Ni/TiO_{2-*anatase*}, and then through a separated bed of 10Ni/TiO_{2-*rutile*}. It is important to note that
 7 in these two configurations the two beds are not in physical contact since they are separated
 8 using quartz wool. The results of this series of experiments are summarized in Table 5.

9
 10 **Table 5.** CO₂ conversion and CH₄ selectivity of two successive beds of 10Ni/TiO_{2-*rutile*} (20%)
 11 and 10Ni/TiO_{2-*anatase*} (80%) and *vice versa* at 260 °C. Conversion and selectivity reported here
 12 are average values for 20 h of TOS.

Configuration	CO ₂ conv. (%)	CH ₄ selec. (%)
C1		
<i>first 10Ni/TiO_{2-<i>rutile</i>} then 10Ni/TiO_{2-<i>anatase</i>}</i>	11 (5.6) ^a	84.4 (78.6) ^a
C2		
<i>first 10Ni/TiO_{2-<i>anatase</i>} then 10Ni/TiO_{2-<i>rutile</i>}</i>	3.5 (5.4) ^a	97.9 (77.1) ^a

13 ^a Expected values (without the synergy) obtained by the simulation of the two successive beds using regressed
 14 kinetic parameters of pure 10Ni/TiO_{2-*rutile*} and pure 10Ni/TiO_{2-*anatase*} are given between brackets.

15
 16 This series of experiments is important since it clearly demonstrated that a physical contact
 17 between the two catalysts is not necessary to obtain the synergistic effect in the case of the
 18 configuration **C1**. Our results contrast significantly with previous studies showing an influence
 19 of the TiO₂ crystallographic phase on CO₂ methanation, since: i) from XPS analyses, activity
 20 does not seem to be linked to a different electronic interaction between Ni and TiO₂ as
 21 previously discussed [33], except maybe at the interface where should be located the active

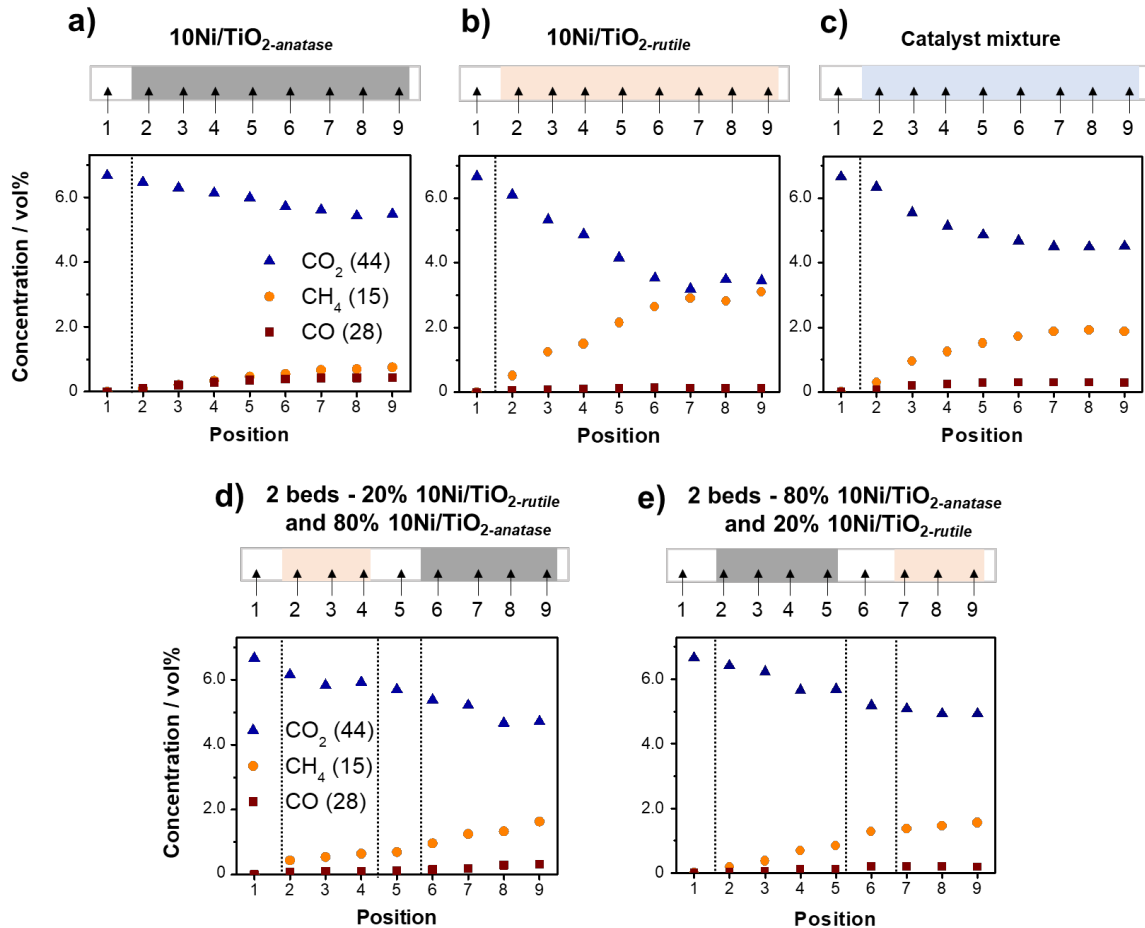
1 sites; and ii) the hypothesis of metal migration [31] is excluded from this latter experiment
2 series.

3 **3.3. Space resolved-gas-sampling analyses.**

4 The following conditions were used for space-resolved gas sampling during CO₂ methanation:
5 $P_{\text{total}} = 1 \text{ bar}$, $T = 340 \text{ }^\circ\text{C}$; $\text{CO}_2/\text{H}_2/\text{He} = 1/4/10$; $\text{WHSV} = 1200 \text{ NmL}_{\text{CO}_2} \text{ h}^{-1} \text{ g}^{-1}$. Under these
6 conditions, CO₂, CH₄, and CO were quantified using an FTIR spectrometer to follow the gas
7 phase composition under different reactor configurations: i) 10Ni/TiO_{2-*anatase*}; ii) 10Ni/TiO_{2-*rutile*};
8 *rutile*; iii) 10Ni/TiO_{2-*anatase*} (80%) +10Ni/TiO_{2-*rutile*} (20%) catalyst mixture; iv) two beds
9 configuration - first 10Ni/TiO_{2-*anatase*} (80%) then 10Ni/TiO_{2-*rutile*} (20%); and v) two beds
10 configuration - first 10Ni/TiO_{2-*rutile*} (20%) then 10Ni/TiO_{2-*anatase*} (80%). The catalytic results
11 (conversion and selectivity) obtained at atmospheric pressure in these experiments as well as in
12 the methanation reactor are presented on Table S9 and Table S10, respectively. The space-
13 resolved gas sampling was performed using a capillary inserted in the catalyst bed (Figure S9)
14 that moved along the axial direction; data were collected for each position along the catalyst
15 using MS. The quantitative results obtained are summarized on Figure 7. This series of
16 experiments shows that 10Ni/TiO_{2-*rutile*} promotes the formation of CH₄ (Figure 7b), while
17 10Ni/TiO_{2-*anatase*} promotes the RWGS reaction with formation of CO, together with CH₄ (Figure
18 7a). When the 2-bed configuration is used, it is observed that: i) in the configuration 10Ni/TiO_{2-*rutile*};
19 *rutile* first, CO₂ methanation occurs first, and then on 10Ni/TiO_{2-*anatase*} RWGS comparably more
20 accelerated; and ii) in the configuration 10Ni/TiO_{2-*anatase*} first, first CO₂ methanation and RWGS
21 take place, the evolved CO on Ni/TiO_{2-*anatase*} does not further react on the Ni/TiO_{2-*rutile*} catalyst
22 that only produces more CH₄ and water. Due to the rather low activity at the atmospheric
23 pressure of this space-resolved gas sampling study, the differences between the two sequential-
24 bed configurations are not large. Nevertheless, the selectivity trends defined by the support

1 structure and also the advantage of the close vicinity of the anatase TiO₂ and rutile TiO₂
 2 supported Ni catalysts on methanation activity is evident (Figure 7c vs. Figures 7d and 7e).

3



4

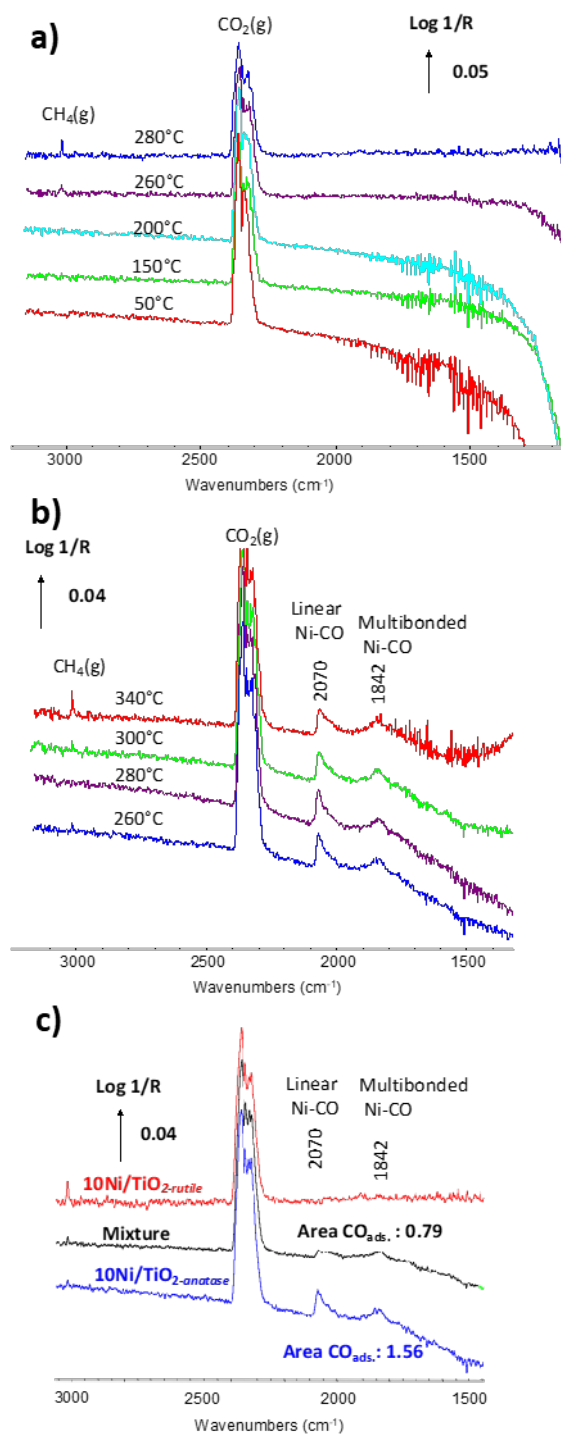
5 **Figure 7.** Space-resolved gas sampling for: a) 10Ni/TiO₂-anatase; b) 10Ni/TiO₂-rutile; c) catalyst
 6 mixture 10Ni/TiO₂-anatase (80%) +10Ni/TiO₂-rutile (20 %); d) 2 beds – 20% 10Ni/TiO₂-rutile and
 7 80% 10Ni/TiO₂-anatase; and e) 2 beds – 80% 10Ni/TiO₂-anatase and 20% 10Ni/TiO₂-rutile. (blue:
 8 CO₂; orange: CH₄; and brown: CO (the contribution from CO₂ has been subtracted)). MS
 9 profiles (a.u.) along the catalyst bed were converted into concentration profiles (in vol. %) by
 10 using the inlet and outlet gas concentrations measured by FTIR.

11

12

1 **3.4 Surface species analysis by DRIFTS operando**

2 For surface species analysis by DRIFTS *operando* during CO₂ methanation, the following
3 conditions were used: P_{total} = 1 bar, T = 280-340 °C; CO₂/H₂ = 1/4; WHSV = 336 NmL_{CO2} h⁻¹
4 g⁻¹. These experiments were performed after reducing the catalyst under H₂ at 400 °C for 1 h.
5 Under these conditions, 10Ni/TiO_{2-*anatase*}, 10Ni/TiO_{2-*rutile*} and the catalyst mixture 80%
6 10Ni/TiO_{2-*anatase*} + 20% 10Ni/TiO_{2-*rutile*} were studied. First, the relative rates were measured at
7 280 °C, and under these conditions, a synergistic effect was also observed, as compared to
8 weighted activities (Figure S10). A series of experiments was also performed at different
9 temperatures to calculate the apparent activation energy (SI.2, Table S7). The calculated
10 activation energies were 80 (10Ni/TiO_{2-*anatase*}), 105 (10Ni/TiO_{2-*rutile*}), 133 (10Ni/TiO_{2-*P25*}) and
11 85.5 kJ.mol⁻¹ (catalyst mixture). Figure 8a shows the spectra for the 10Ni/TiO_{2-*rutile*} catalyst at
12 various temperatures between 50 and 280 °C taken in the DRIFTS cell under a CO₂+H₂ feed.
13 Only the large band of CO₂(g) at 2360 cm⁻¹ is visible for all the temperatures, whereas the
14 CH₄(g) band at 3050 cm⁻¹ starts to appear at 260 °C. There are no visible surface species on
15 10Ni/TiO_{2-*rutile*}. If, at 280 °C, H₂ is removed from the gas mixture, two large bands at 1875 and
16 2024 cm⁻¹ appear, characteristic of multi-bonded and linear CO on Ni, respectively. These
17 bands disappeared when H₂ was added again to the gas mixture, meaning that nickel carbonyl
18 species are reversibly formed when H₂ is removed (Figure S11). DRIFTS spectra were also
19 recorded at various temperatures with 10Ni/TiO_{2-*anatase*} (Figure 8b). In that case, carbonyls
20 adsorbed on Ni are visible under a CO₂+H₂ feed, exhibiting two characteristic bands at 1842
21 cm⁻¹ for multi-bonded nickel carbonyl and 2070 cm⁻¹ for linear nickel carbonyl species.
22 Surprisingly, the CO adsorbed on Ni with the mixture of H₂/CO₂ is slowly removed when H₂
23 is not present in the gas mixture (Figure S12). Ni-CO species are still present 5 min after
24 removing H₂, and they only disappear after 4 h.



1

2 **Figure 8** DRIFTS spectra recorded under 2% CO₂ + 8% H₂ (1 bar) for: a) 10Ni/TiO_{2-rutile} at
 3 various temperatures; b) 10Ni/TiO_{2-anatase} at various temperatures; and c) 10Ni/TiO_{2-rutile},
 4 10Ni/TiO_{2-anatase} and the catalyst mixture 80% 10Ni/TiO_{2-anatase} + 20% 10Ni/TiO_{2-rutile} at 280°C.
 5 (WHSV = 336 NmL_{CO2} h⁻¹ g⁻¹).

6

1 This contrasts with the data collected over the 10Ni/TiO_{2-rutile} catalyst, possibly due to
2 differences in CO₂ adsorption or dissociation rates or CO desorption rate (and the gradual
3 oxidation of Ni particles by CO₂ in the absence of H₂). There is no visible formation of formate
4 or carbonate species on nickel. These results contrast with those obtained by Bao *et al.* at much
5 lower temperature (*i.e.* 75 °C) [33], who observed the formation of hydrogenocarbonate species
6 on both Ni/TiO_{2-rutile} and Ni/TiO_{2-anatase} catalysts. The higher temperatures used here likely led
7 to lower surface coverage of these weakly bound species. The study by Bao *et al.* was also
8 conducted at atmospheric pressure, but using a catalyst reduced 4 h at 500°C and at a higher
9 WHSV (2400 NmL_{CO2} g⁻¹ h⁻¹). The fact that such adsorbed species were not observed in this
10 study could thus be related to: i) a low surface coverage; or ii) the reduction conditions. For this
11 latter possibility, Panagiotopoulou *et al.* have recently shown that during CO₂ methanation
12 formate species appeared after prolonged catalyst reduction [62]. The same operando DRIFTS
13 experiments were performed with the mixture of catalysts. Figure 8c shows a comparison of
14 the three catalysts. A quantitative analysis of the sample spectra at 280 °C (Figure 8.c) is only
15 valid if the materials exhibit similar scattering and absorption coefficient, leading to similar
16 optical pathlengths. This can be assumed to be true in the present case, since a mixture of the
17 same loading of Ni supported on two titania polymorphs are considered. For the catalyst
18 mixture 80% 10Ni/TiO_{2-anatase} + 20% 10Ni/TiO_{2-rutile}, CO adsorbed on metallic Ni is still visible,
19 but the band area of adsorbed CO has a calculated value of 0.79 for the mixture, when a value
20 of 1.25 (= 0.8 * 1.56) would be expected for an 80% dilution of the signal obtained on the pure
21 10Ni/TiO_{2-anatase}. This important observation corroborates the fact that the 10Ni/TiO_{2-rutile}
22 assisted the hydrogenation of the CO(ads) on the 10Ni/TiO_{2-anatase}. This result enables to unravel
23 the origin of one of the synergetic effects between 10Ni/TiO_{2-rutile} and 10Ni/TiO_{2-anatase}.

24

25

1 **3.5 H₂-TPD experiments and catalytic tests to assess hydrogen spillover**

2 The results from catalyst characterization, catalytic study, operando DRIFTS and MS study can
3 be summarized as follows:

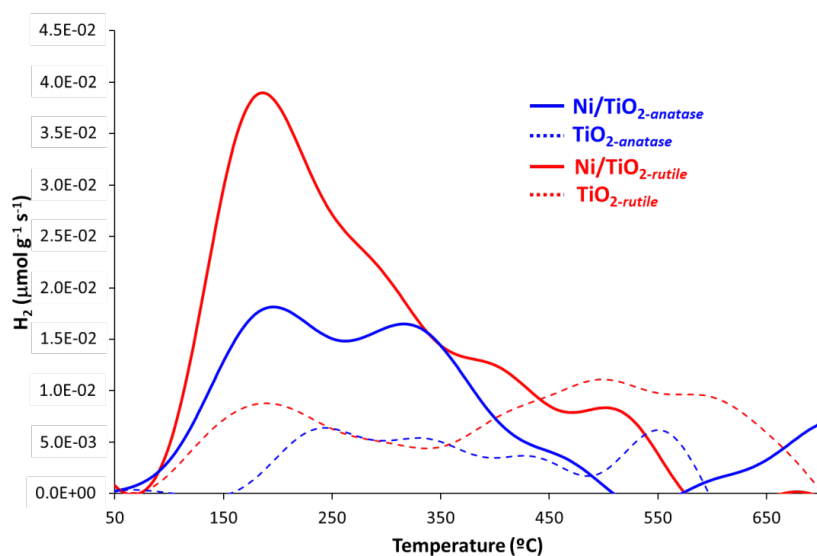
- 4 - 10Ni/TiO_{2-*anatase*} and 10Ni/TiO_{2-*rutile*} present similar Ni particle size before and after
5 catalysis, and from XPS analyses, similar metal support interactions (except maybe at
6 the interface where should be located the active sites);
- 7 - for pure catalysts, the activity, selectivity and stability for CO₂ methanation are higher
8 on Ni/TiO_{2-*rutile*} than those on 10Ni/TiO_{2-*anatase*};
- 9 - when a mixture of these two catalysts is used, a synergistic effect is observed, since the
10 measured rate of the mixture is higher than the corresponding calculated weighted rate;
- 11 - the two catalysts do not need to be in physical contact for the synergistic effect to occur
12 (configuration **C1**);
- 13 - during the methanation reaction, adsorbed CO is accumulating on Ni/TiO_{2-*anatase*}, and
14 one role of the Ni/TiO_{2-*rutile*} could be to assist the hydrogenation of this adsorbed CO.

15
16 Taken together, these results suggest that: i) these catalysts could contain mainly interfacial
17 actives sites; ii) Ni/TiO_{2-*anatase*} is a more selective but less active RWGS reaction catalyst
18 compared to Ni/TiO_{2-*rutile*} (hypothesis independently checked, see Figure S12), which is a
19 necessary step for methanation; iii) methanation of CO, generally recognized as the rate-
20 determining step of the reaction [30, 63-66], should be faster on Ni/TiO_{2-*rutile*} [33], iv) hydrogen
21 spillover, which occurs fast and at relatively large distances on reducible supports, by surface
22 species but also by gas-phase radicals [67-69], could be involved in the process, by assisting
23 the CO₂ hydrogenation steps on Ni/TiO_{2-*anatase*}; and v) the optimal anatase/rutile ratio can arise
24 from the balance of the reaction rates for the H-spillover and CO₂ methanation.

1 Concerning hydrogen spillover, it is worth mentioning that it has already been proposed as the
2 explanation of the synergy between Pd/ γ -Al₂O₃ and Rh/ γ -Al₂O₃ catalysts in CO₂ methanation
3 [70]. In that study, the authors have shown that although Pd/ γ -Al₂O₃ is inactive at 200 °C, the
4 activity of mechanical mixtures of the two catalysts was up to 50 % higher than that of the pure
5 Rh/ γ -Al₂O₃ catalyst. While Pd/ γ -Al₂O₃ alone could not hydrogenate the Pd-CO adsorbed
6 species, the presence of Rh/ γ -Al₂O₃ significantly increased the reactivity of Pd-CO species,
7 which was proposed to account for the observed synergistic effect, *via* hydrogen spillover.
8 Synergies associated to H-spillover were also reported for mechanical mixtures of Rh/ γ -Al₂O₃
9 (methanation catalyst) and Ni/C (spillover catalyst) [71], for Ni-Ru/SiO₂-La₂O₃ catalysts (Ni:
10 methanation catalyst, and Ru: spillover catalyst) [72], or for Co-Pt/SiO₂ catalysts [73, 74]. In
11 this latter case, it was shown that the H-spillover (from Pt to Co) significantly enhance the
12 reduction of Co. This effect could be also important in our case since: i) it is known that Ni
13 deactivation can occur due to coke formation [75] or formation of Ni-hydroxide by reaction
14 with water [63], and ii) the deactivation observed for pure Ni/TiO_{2-*anatase*} is suppressed when
15 using the catalyst mixture (see Figure S7). Another implication of H-spillover in CO₂
16 methanation on Ru/CeO₂ [76] and Ni/MgO [77] catalysts is related to H-assisted H₂O removal.
17 H₂-TPD of the three catalysts, 10Ni/TiO_{2-*anatase*}, 10Ni/TiO_{2-*rutile*} and the physical mixture, were
18 performed after hydrogen reduction at 400 °C in order to quantify the spillover of hydrogen.
19 The total amounts of H₂ adsorbed on these three catalysts were 29.6, 50.3 and 32.9 $\mu\text{mol}\cdot\text{g}^{-1}$ for
20 10Ni/TiO_{2-*anatase*}, 10Ni/TiO_{2-*rutile*} and the mixture, respectively. Concerning the supports (Figure
21 9), higher amounts of H₂ were observed for the TiO_{2-*rutile*} (4 m² g⁻¹) than for TiO_{2-*anatase*} (10 m²
22 g⁻¹). The heterolytic H₂ dissociation (leading to a hydride and a hydroxyl) on TiO_{2-*rutile*} has been
23 reported to proceed much more easily ($E_a = 8.5 \text{ kcal mol}^{-1}$) than on TiO_{2-*anatase*} ($E_a = 24 \text{ kcal}$
24 mol⁻¹) [78]. For TiO_{2-*rutile*}, the hydride produced by the H₂ heterolytic activation can transfer
25 from Ti to O with activation energy of 22.8 kcal mol⁻¹, yielding the homolytic products. For the

1 catalysts, higher amounts of H₂ were observed for the 10Ni/TiO_{2-rutile} compared to 10Ni/TiO₂₋
2 *anatase*. Theoretical calculations have shown that although H₂ desorption is difficult on a
3 stoichiometric TiO₂ surface, it becomes easier (and favored upon H₂O desorption) with an
4 increase in O_v, which are generated by H₂O desorption [79]. Two main desorption peaks are
5 observed at ~190 and ~300 °C. The presence of these two peaks in Ni/TiO₂ catalysts has already
6 been reported [80]. The peak at lower temperature (190 °C) can be attributed to hydrogen
7 chemisorbed at the surface of the Ni particles [20], and to reverse hydrogen spillover. The
8 presence of a peak at higher temperatures has been discussed in several studies dealing with
9 hydrogen spillover on TiO₂ supports, it is ascribed to H-spillover associated with the support
10 [81, 82]. The desorption of hydrogen adsorbed at interfacial sites located at the metal-support
11 interface has also be invoked [83]. These analyses point to a higher H-spillover on 10Ni/TiO₂₋
12 *rutile* than on 10Ni/TiO_{2-anatase}. On Ru/TiO₂ catalysts, the opposite situation was observed [53],
13 which highlights the importance of the intimate interaction between the metal and the support
14 on the jump of the hydride from the metal to the support.

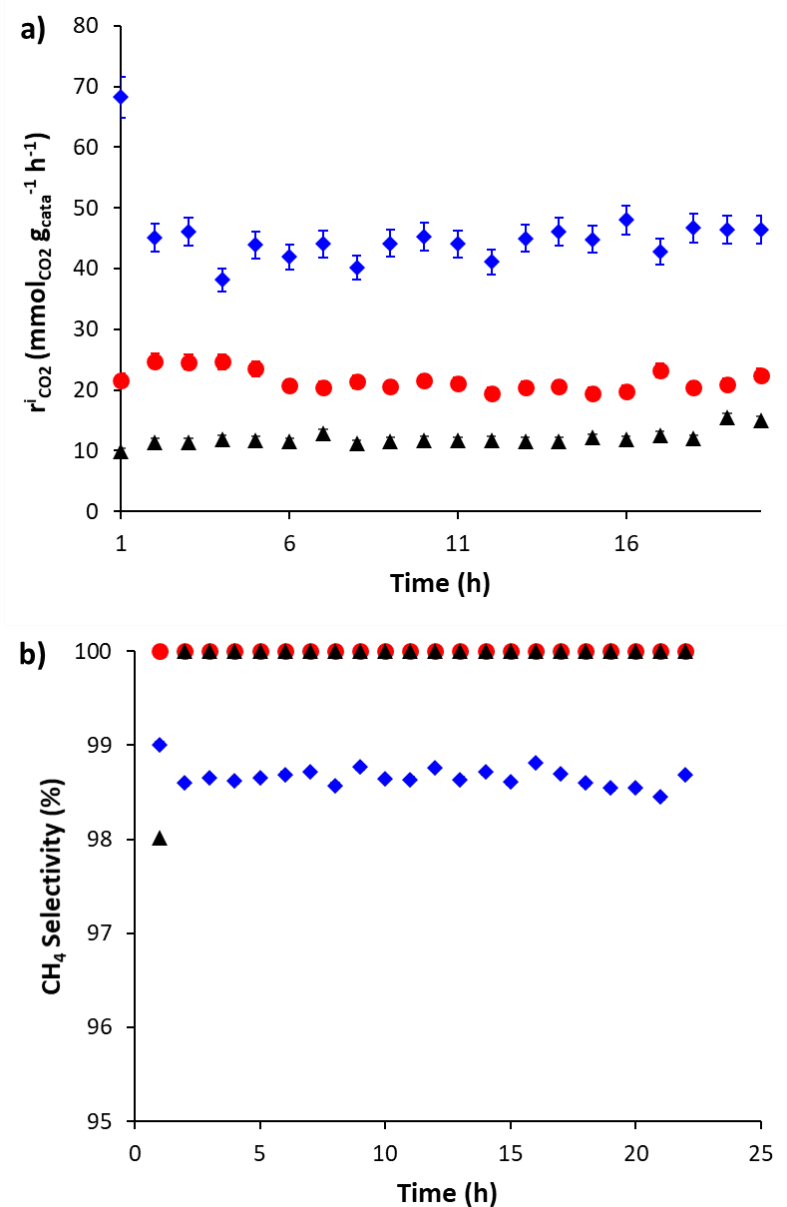
15



16

17 **Figure 9.** H₂-TPD profiles over TiO_{2-anatase}, 10Ni/TiO_{2-anatase}, TiO_{2-rutile} and 10Ni/TiO_{2-rutile}.

1



2

3 **Figure 10.** Comparison of: a) CO₂ consumption rates at the inlet of the reactor; and b) CH₄
 4 selectivity at 260 °C of 10Ni/TiO₂-P25 diluted with 1.8 g of SiC (black triangles), diluted in TiO₂-
 5 *rutile* (red circles) - 0.2g 10Ni/TiO₂-P25 + 1g TiO₂-*rutile* (+ 0.8 g SiC), and diluted in TiO₂-*anatase*
 6 (blue diamonds) - 0.2g 10Ni/TiO₂-P25 + 1g TiO₂-*anatase* (+ 0.8 g SiC).

7

1 Since spillover is often postulated when a dilution of the catalyst leads to an activity increase,
2 we performed two experiments starting from the 10Ni/TiO_{2-P25} catalyst, measuring the CO₂
3 consumption rate evolution upon dilution of the catalyst with either TiO_{2-rutile} or TiO_{2-anatase} (in
4 addition to SiC). The increase of the rate with higher degrees of dilution can be understood if
5 one admits that the reaction also involves the support (because of spillover hydrogen) in
6 addition to reactivity occurring on the sites of the Ni/TiO₂ particles. The results of these
7 experiments performed at 260 °C in order to better quantify differences are shown on Figure
8 10 and Table S11.

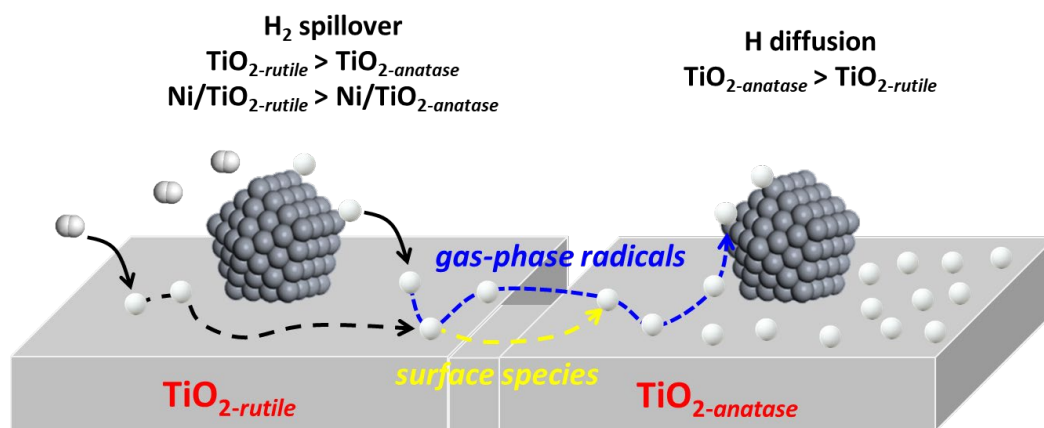
9 For both tests performed with diluted catalysts, the rate increases, confirming hydrogen
10 spillover. The rate increase is significantly higher when the dilution is performed with the TiO₂₋
11 *anatase* support, with a calculated TOF = 0.0197 s⁻¹, which is one of the highest reported for Ni-
12 catalyzed CO₂ methanation at this temperature and GHSV (see Table S12 for comparison with
13 reference catalysts). We independently verified that an increase in CO₂ consumption rates was
14 also observed after dilution of the 10Ni/TiO_{2-rutile} catalyst in pure TiO_{2-anatase} support (Figure
15 S14 and Table S13). These data suggest that CO₂ is also hydrogenated on the Ni-free TiO₂₋
16 *anatase* and much less on the Ni-free TiO_{2-rutile}. On TiO_{2-anatase}, however, the reaction seems to be
17 slightly less selective (Table S11) since small amounts of CO are produced.

18 These results can be rationalized by: i) an easier spillover hydrogen species diffusion on TiO₂₋
19 *anatase* than on TiO_{2-rutile} and/or ii) the higher specific surface area of TiO_{2-anatase} (10 m² g⁻¹)
20 compared to TiO_{2-rutile} (4 m² g⁻¹). To evaluate the impact of the support surface area we also
21 performed a dilution test with the 10Ni/TiO_{2-P25} catalyst and only 0.4 g of TiO_{2-anatase} to be at
22 isosurface with 1 g of TiO_{2-rutile} (Table S11). In that case the CO₂ consumption rate increases
23 compared to pure 10Ni/TiO_{2-P25} (15.0 mmol_{CO2} g_{cat}⁻¹ h⁻¹) is not so high. Indeed, the rate is 25.0
24 mmol_{CO2} g_{cat}⁻¹ h⁻¹ (0.4 g of TiO_{2-anatase}) instead of 45.4 mmol_{CO2} g_{cat}⁻¹ h⁻¹ (1 g of TiO_{2-anatase}), which
25 is still higher than with 1 g of TiO_{2-rutile} (21.3 mmol_{CO2} g_{cat}⁻¹ h⁻¹).

1 If the bare supports are considered, the mechanism for hydrogen atom diffusion has been
2 investigated by DFT [84-86]. Three competing processes have been taken into account, namely,
3 migration of H on the surface, diffusion of H into the bulk, and hydrogen desorption. On both
4 supports, diffusion of H into the bulk is both kinetically and thermodynamically favorable.
5 Activation barriers for bulk migration of 102 and 67 kJ mol⁻¹ have been reported for TiO₂-*rutile*
6 and TiO₂-*anatase*, respectively. This latter result corroborates our experimental findings. We can
7 thus propose that Ni-initiated hydrogen spillover on Ni/TiO₂ creates active sites on the TiO₂
8 bare support for CO₂ hydrogenation. The generation thanks to H-spillover of active
9 hydrogenation sites on TiO₂ (O_v created by partial reduction of TiO₂) has already been reported
10 during the Ag/TiO₂ catalyzed hydrodeoxygenation of guaiacol [87] and the Fe/TiO₂ catalyzed
11 ammonia synthesis [88].

12 It thus appears that the origin of the synergetic effect between TiO₂ crystalline phases in the
13 Ni/TiO₂ catalyzed CO₂ methanation reaction comes from hydrogen activation. The Ni/TiO₂-
14 *rutile* catalyst is much more active for CO₂ reduction to methane than Ni/TiO₂-*anatase* for a CO₂/H₂
15 ratio of 1/4 and 1/1. On the other hand, Ni/TiO₂-*anatase* is more selective for the RWGS reaction
16 catalyst, and the diffusion of H-species is easier on the TiO₂-*anatase* support than on TiO₂-*rutile*.
17 Thus, in a catalyst mixture, the H-species resulting from the spillover on the Ni/TiO₂-*rutile*
18 catalyst should have the tendency to accumulate on the TiO₂-*anatase* support (Scheme 1).

19 The contact between the two supports is actually not necessary since gas phase hydrogen
20 spillover can occur [66-68, 89-91]. Even if thermodynamically the gas phase H spillover
21 concentration should be very low [92], it should permit a fast formation of H species adsorbed
22 on the support. Additionally, the water present in the gas phase could be involved in the
23 transport process maybe *via* the reactor walls or the quartz wool used to separate the catalyst
24 beds [93].



1
 2 **Scheme 1.** Hydrogen spillover and H diffusion in a Ni/TiO_{2-rutile} - Ni/TiO_{2-anatase} catalyst
 3 mixture.

4
 5 When these H species have reached the TiO_{2-anatase} support, the CO₂ hydrogenation is greatly
 6 improved on the Ni/TiO_{2-anatase} catalyst, the methane being formed even from the support alone,
 7 and catalyst deactivation is reduced. The part of CH₄ formed directly on the TiO₂ support is
 8 however relatively low. Thus, we compare the CO₂ conversion at 260 °C for the 10Ni/TiO_{2-rutile}
 9 catalyst (200 mg), the 10Ni/TiO_{2-rutile} catalyst (60 mg, corresponding to 30% in weight) mixed
 10 with 140 mg of TiO_{2-anatase} (corresponding to 70% in weight), and the Ni/TiO_{2-rutile} catalyst (60
 11 mg, corresponding to 30% in weight) mixed with 140 mg of Ni/TiO_{2-anatase} (corresponding to
 12 70% in weight). The results, presented on Table S13, clearly show that the conversion
 13 improvement linked to the Ni on Ni/TiO_{2-anatase} is much higher than the one linked to the TiO₂₋
 14 *anatase* support itself. The precise role of the H species is still unclear, but it is worth mentioning
 15 that TiO₂ reduction by hydrogen spillover has been reported [94-96]. Additionally, it was
 16 reported that on Rh catalyst supported on CeO₂ (another reducible support), the fraction of CO
 17 that undergoes dissociation increases significantly as the CeO₂ surface is reduced [97]. The fact
 18 that the TOF of the catalyst mixture is significantly higher than that of the Ni/TiO_{2-P25} catalyst
 19 could be related to the lower specific surface area of the supports used in the mixture compared

1 to TiO_{2-P25}, and to Ni particle proximity, which should be higher for the mixture of catalysts.
2 These two characteristics should favor the hydrogen spillover. Finally, considering the fact that
3 Ni particles in Ni/TiO_{2-anatase} and Ni/TiO_{2-rutile} catalysts present similar sizes without TiO_x
4 overlayers, and similar electronic interaction with the supports, we can propose that these
5 catalysts should contain mainly interfacial active sites [98]. The importance of the metal-
6 support interface in Ni-catalyzed CO₂ hydrogenation has been discussed [57,77,99,100]. For
7 CO₂ methanation, the role of the active sites located at the Ni-support interface has been studied
8 by DFT and *operando* DRIFT analyses, and different implications related to the reaction
9 mechanism have been proposed.

10 On Ni/ZrO₂ catalysts, hydrogen species generated by hydrogen spillover could contribute to the
11 formation of O_v on the ZrO₂ surface, which enhance CO₂ adsorption and activation [99]. It was
12 also proposed that the interaction of the Ni-ZrO₂ interface with adsorbed CO was strong enough
13 to facilitate its further hydrogenation to CH₄ [57]. For the Sabatier reaction on Ni/MgO
14 catalysts, it was shown by DFT that the presence of the MgO support is beneficial for the OH
15 removal from intermediate species, and consequently for H₂O formation during CO₂
16 methanation, due to hydrogen-spillover and the strong OH adsorption on the MgO support [77].

17 On Ni/CeO₂ catalysts [101], it was recently proposed that, as in the case of Ni/ZrO₂ catalysts
18 [99], H-spillover from Ni to CeO₂ can lead to a partial reduction of CeO₂ and generation of O_v
19 at the metal-support interface region. A linear correlation between the CO₂ methanation
20 reaction rate and the number of O_v was reported. This suggests the involvement of surface O_v
21 in CO₂ adsorption and activation [102]. A similar phenomenon could occur on TiO₂, another
22 reducible oxide. Such a phenomenon could be at the origin of the difference of reactivity
23 between 10Ni/TiO_{2-anatase} and 10Ni/TiO_{2-rutile} catalysts. Indeed, it was shown by DFT that the
24 O_v formation energy is much lower on TiO_{2-rutile} rutile than on TiO_{2-anatase} [103]. Thus, the

1 higher H-spillover on 10Ni/TiO_{2-rutile} than on 10Ni/TiO_{2-anatase} could result in a higher
2 concentration of O_v on the 10Ni/TiO_{2-rutile} catalyst, and consequently a higher activity.

3 Finally, as far as Ni/TiO₂ catalyst stability is concerned, it is worth mentioning that it has been
4 reported that highly active hydrogen species resulting from spillover that diffuse on Ni catalyst
5 surface lead to the hydrogenation of the coke precursor species adsorbed on the catalyst
6 [104,105], and to the reduction of nickel oxide [106]. Such phenomena could explain why the
7 use of mixture of TiO₂ phases allows limiting catalyst deactivation (Fig. S6b for 10Ni/TiO₂₋
8 *P25*).

9

10 **4. Conclusion**

11 Nickel catalysts (10% w/w) were prepared on TiO_{2-rutile}, TiO_{2-anatase} and TiO_{2-P25}. The catalysts
12 prepared on TiO_{2-rutile} and TiO_{2-anatase} present a similar Ni particle size (~ 30 nm) before and
13 after CO₂ methanation, as well as similar metal-support interactions. The 10Ni/TiO_{2-P25} presents
14 smaller particle size (~ 20 nm). The CO₂ consumption rate measured at the inlet of the reactor
15 of 10Ni/TiO_{2-anatase}, 10Ni/TiO_{2-rutile}, 10Ni/TiO_{2-P25} and a physical mixture of 30% 10Ni/TiO₂₋
16 *rutile* + 70% 10Ni/TiO_{2-anatase} show that a synergistic effect operates when a mixture of the crystal
17 phases of TiO₂ is used as a support in the Ni/TiO₂-catalyzed methanation reaction. The synergy
18 observed using a mixture of catalysts could also occur *even if the two catalysts are not in*
19 *physical contact*. H₂-TPD analyses and methanation tests performed with diluted catalysts have
20 shown that hydrogen spillover is more pronounced on the Ni/TiO_{2-rutile} catalyst. DRIFTS
21 operando analyses have shown that adsorbed CO is accumulating on Ni/TiO_{2-anatase} but not on
22 Ni/TiO_{2-rutile}. The synergy between the two catalysts can be rationalized as follows: i) the
23 Ni/TiO_{2-rutile} catalyst is active and selective for CO₂ methanation and also for hydrogen
24 activation; ii) the Ni/TiO_{2-anatase} is poorly active for the CO₂ methanation and RWGS, and the

1 TiO_{2-*anatase*} support is more efficient than TiO_{2-*rutile*} for diffusion of H species; iii) when the two
2 catalysts are used together, the H species diffuse from Ni/TiO_{2-*rutile*} to Ni/TiO_{2-*anatase*}; iv) the H-
3 enriched Ni/TiO_{2-*anatase*} catalyst becomes very active for CO₂ methanation. The optimal TiO_{2-*anatase*}-
4 TiO_{2-*rutile*} ratio (between 0.4 and 0.8) is achieved through a control of the balance of the
5 spillover, CO₂ methanation and deactivation rates. Finally, the higher TOF obtained with
6 catalyst mixtures compared to Ni/TiO_{2-*P25*} suggests that interfacial sites, presumably involving
7 O_v, should be involved in this reaction. Our results that confirm the essential role of the support
8 for Ni-based CO₂ methanation catalysts [107], can also be put into perspective to propose an
9 explanation of the support effect (*rutile vs anatase*) observed on Co/TiO₂ catalysts for Fischer-
10 Tropsch synthesis, for which a similar synergistic effect has been observed without being
11 clearly explained [108, 109]. DFT calculations are in course to reveal the mechanism of the
12 hydrogenation at the interfacial active sites and on the bare TiO_{2-*anatase*} support, and to clarify
13 the possible role(s) of the H species resulting from spillover (H-assisted hydrogenation steps,
14 H-assisted water desorption or H-assisted Ni reduction).

15 **Notes**

16 The authors declare no competing financial interest.

17

18 **Acknowledgements.**

19 This work was financially supported by “Région Occitanie” through a laboratory and company
20 contract “HYDROMET: Renewable CO₂ hydrogenation for methane production”
21 (N°15065590). B.F.M. acknowledges the exploratory project under the Fundação para a
22 Ciência e a Tecnologia (FCT, Portugal) Investigator Programme (ref. IF/00301/2015) with
23 financial support from FCT/MCTES, through national funds (PIDDAC).

24

1 **References:**

- 2 [1] D. Y. C. Leung, G. Caramanna, M. M. Maroto-Valer, An overview of current status of
3 carbon dioxide capture and storage technologies, *Renew. Sus. Energ. Rev.*, 39 (2014)
4 426-443.
- 5 [2] M. Bui, C. S. Adjiman, A. Bardow, E. J. Anthony, A. Boston, S. Brown, P. S. Fennell,
6 S. Fuss, A. Galindo, L. A. Hackett, et al. Carbon capture and storage (CCS): the way
7 forward, *Energy Environ. Sci.*, 11 (2018) 1062-1176.
- 8 [3] J. G. Vitillo, B. Smit, L. Gagliardi, Introduction: Carbon Capture and Separation,
9 *Chem. Rev.*, 117 (2017) 9521-9523.
- 10 [4] M. Mikkelsen, M. Jørgensen, F. C. Krebs, The teraton challenge. A review of fixation
11 and transformation of carbon dioxide, *Energy Environ. Sci.*, 3 (2010) 43-81.
- 12 [5] T. Sakakura, J.-C. Choi, H. Yasuda, Transformation of Carbon Dioxide, *Chem. Rev.*,
13 107 (2007) 2365-2387.
- 14 [6] J. Artz, T. E. Müller, K. Thenert, J. Kleinekorte, R. Meys, A. Sternberg, A. Bardow,
15 W. Leitner, Sustainable Conversion of Carbon Dioxide: An Integrated Review of
16 Catalysis and Life Cycle Assessment, *Chem. Rev.*, 118 (2018) 434-504.
- 17 [7] G. Centi, S. Perathoner, Opportunities and prospects in the chemical recycling of
18 carbon dioxide to fuels, *Catal. Today*, 148 (2009) 191-205.
- 19 [8] K. Ghaib, K. Nitz, F.-Z. Ben-Fares, Chemical Methanation of CO₂: A Review,
20 *ChemBioEng Rev.*, 3 (2016) 266-275.
- 21 [9] P. Frontera, A. Macario, M. Ferraro, P. Antonucci, Supported Catalysts for CO₂
22 Methanation: A Review, *Catalysts*, 7 (2017) 59.
- 23 [10] W. Wei, G. Jinlong, Methanation of carbon dioxide: an overview, *Front. Chem. Sci.*
24 *Eng.*, 5 (2011) 2-10.

- 1 [11] A. Solis-Garcia, J. C. Fierro-Gonzalez, Mechanistic Insights into the CO₂ Methanation
2 Catalyzed by Supported Metals: A Review, *J. Nanosci. Nanotechnol.*, 19 (2019)
3 3110-3123.
- 4 [12] M. Bailera, P. Lisbona, L. M. Romeo, S. Espatolero, Power to Gas projects review:
5 Lab, pilot and demo plants for storing renewable energy and CO₂, *Renew. Sus. Energ.*
6 *Rev.*, 69 (2017) 292-312.
- 7 [13] K. Ghaib, F.-Z. Ben-Fares, Power-to-Methane: A state-of-the-art review, *Renew. Sus.*
8 *Energ. Rev.*, 81 (2018) 433-446.
- 9 [14] M. Thema, F. Bauer, M. Sterner, Power-to-Gas: Electrolysis and methanation status
10 review, *Renew. Sus. Energ. Rev.*, 112 (2019) 775-787.
- 11 [15] X. Guo, A. Traitangwong, M. Hu, C. Zuo, V. Meeyoo, Z. Peng, C. Li, Carbon Dioxide
12 Methanation over Nickel-Based Catalysts Supported on Various Mesoporous Material,
13 *Energ. Fuels*, 32 (2018) 3681-3689.
- 14 [16] J. Martínez, E. Hernández, S. Alfaro, R. López Medina, G. Valverde Aguilar, E.
15 Albiter, M. A. Valenzuela, High Selectivity and Stability of Nickel Catalysts for CO₂
16 Methanation: Support Effects, *Catalysts*, 9 (2018) 24.
- 17 [17] K. Stangeland, D. Kalai, H. Li, Z. Yu, CO₂ Methanation: The Effect of Catalysts and
18 Reaction Conditions, *Energy Procedia*, 105 (2017) 2022-2027.
- 19 [18] I. Sreedhar, Y. Varun, S. A. Singh, A. Venugopal, B. M. Reddy, Developmental trends
20 in CO₂ methanation using various catalysts, *Catal. Sci. Technol.*, 9 (2019) 4478-4504.
- 21 [19] J. H. Jensen, J. M. Poulsen, N. U. Andersen, From coal to clean energy,
22 Nitrogen+Syngas, (2011) 310.
- 23 [20] J. Liu, C. Li, F. Wang, S. He, H. Chen, Y. Zhao, M. Wei, D. G. Evans, X. Duan,
24 Enhanced low-temperature activity of CO₂ methanation over highly-dispersed Ni/TiO₂
25 catalyst, *Catal. Sci. Technol.*, 3 (2013) 2627-2633.

- 1 [21] Y. Wang, Y. Xu, Q. Liu, J. Sun, S. Ji, Z.-j. Wang, Enhanced low-temperature activity
2 for CO₂ methanation over NiMgAl/SiC composite catalysts, *J. Chem. Technol.*
3 *Biotechnol.*, 94 (2019) 3780-3786.
- 4 [22] S. Tada, T. Shimizu, H. Kameyama, T. Haneda, R. Kikuchi, Ni/CeO₂ catalysts with
5 high CO₂ methanation activity and high CH₄ selectivity at low temperatures, *Int. J.*
6 *Hydrogen Energ.*, 37 (2012) 5527-5531.
- 7 [23] L. Bian, L. Zhang, R. Xia, Z. Li, Enhanced low-temperature CO₂ methanation activity
8 on plasma-prepared Ni-based catalyst, *J. Nat. Gas Sci. Eng.*, 27 (2015) 1189-1194.
- 9 [24] W. L. Vrijburg, E. Moiola, W. Chen, M. Zhang, B. J. P. Terlingen, B. Zijlstra, I. A. W.
10 Filot, A. Züttel, E. A. Pidko, E. J. M. Hensen, Efficient Base-Metal NiMn/TiO₂
11 Catalyst for CO₂ Methanation, *ACS Catal.*, 9 (2019) 7823-7839.
- 12 [25] X. Guo, H. He, A. Traitangwong, M. Gong, V. Meeyoo, P. Li, C. Li, Z. Peng, S.
13 Zhang, Ceria Imparts Superior Low Temperature Activity to Nickel Catalysts for CO₂
14 Methanation, *Catal. Sci. Technol.*, 9 (2019) 5636-5650.
- 15 [26] S. Bagheri, N. Muhd Julkapli, S. Bee Abd Hamid, Titanium Dioxide as a Catalyst
16 Support in Heterogeneous Catalysis, *Sci. World J.*, (2014) 727496.
- 17 [27] K. Bourikas, C. Kordulis, A. Lycourghiotis, Titanium Dioxide (Anatase and Rutile):
18 Surface Chemistry, Liquid–Solid Interface Chemistry, and Scientific Synthesis of
19 Supported Catalysts, *Chem. Rev.*, 114 (2014) 9754-9823.
- 20 [28] U. Diebold, The Surface Science of Titanium Dioxide, *Surf. Sci. Rep.*, 48 (2003) 53-
21 229.
- 22 [29] W. Li, G. Zhang, X. Jiang, Y. Liu, J. Zhu, F. Ding, Z. Liu, X. Guo, C. Song, CO₂
23 Hydrogenation on Unpromoted and M-Promoted Co/TiO₂ Catalysts (M = Zr, K, Cs):
24 Effects of Crystal Phase of Supports and Metal – Support Interaction on Tuning
25 Product Distribution, *ACS Catal.*, 9 (2019) 2739-2751.

- 1 [30] M. R. Prairie, A. Renken, J. G. Highfield, K. Ravindranathan Thampi, M. Grätzel, A
2 fourier transform infrared spectroscopic study of CO₂ methanation on supported
3 ruthenium, *J. Catal.*, 129 (1991) 130-144.
- 4 [31] A. Kim, C. Sanchez, G. Patriarche, O. Ersen, S. Moldovan, A. Wisnet, C. Sassoze, D.
5 P. Debecker, Selective CO₂ methanation on Ru/TiO₂ catalysts: unravelling the
6 decisive role of the TiO₂ support crystal structure, *Catal. Sci. Technol.*, 6 (2016) 8117-
7 8128.
- 8 [32] A. Kim, D. P. Debecker, F. Devred, V. Dubois, C. Sanchez, C. Sassoze, CO₂
9 methanation on Ru/TiO₂ catalysts: On the effect of mixing anatase and rutile TiO₂
10 supports, *Appl. Catal. B.*, 220 (2018) 615-625.
- 11 [33] Y. Lin, Y. Zhu, X. Pan, X. Bao, Modulating the methanation activity of Ni by the
12 crystal phase of TiO₂, *Catal. Sci. Technol.*, 7 (2017) 2813-2818.
- 13 [34] S. Chai, Y. Men, J. Wang, S. Liu, Q. Song, W. An, G. Kolb, Boosting CO₂
14 Methanation Activity on Ru/TiO₂ Catalysts by Exposing (001) Facets of Anatase
15 TiO₂, *J. CO₂ Util.*, 33 (2019) 242-252.
- 16 [35] A. Borodzinski, M. Bonarowska, Relation between Crystallite Size and Dispersion on
17 Supported Metal Catalysts, *Langmuir*, 13 (1997) 5613-5620.
- 18 [36] A. Champon, A. Bengaouer, S. Chaise, S. Thomas, A.-C. Roger, Carbon dioxide
19 methanation kinetic model on a commercial Ni/Al₂O₃ catalyst, *J. CO₂ Util.*, 34 (2019)
20 256-265.
- 21 [37] K. J. A. Raj, M. G. Prakash, R. Mahalakshmy, T. Elangovan, B. Viswanathan, Liquid
22 Phase Hydrogenation of Nitrobenzene over Nickel Supported on Titania, *Chin. J.*
23 *Catal.*, 33 (2012) 1299–1305.

- 1 [38] M. Xu, S. He, H. Chen, G. Cui, L. Zheng, B. Wang, M. Wei, TiO_{2-x}-modified Ni
2 nanocatalyst with tunable metal-support interaction for water-gas shift reaction, ACS
3 Catal., 7 (2017) 7600-7609.
- 4 [39] A. Shukla, R. Kumar Singha, T. Sasaki, S. Adak, S. Bhandari, V. V. D. N. Prasad, A.
5 Bordoloi, R. Bal, Room temperature selective reduction of nitroarenes to azoxy
6 compounds over Ni-TiO₂ catalyst, Mol. Catal. 490 (2020) 110943.
- 7 [40] G. Sankar, K. R. Kannan, C. N. R. Rao, Anatase-Rutile Transformation in Fe/TiO₂,
8 Th/TiO₂ and Cu/TiO₂ Catalysts and its Possible Role in Metal-Support Interaction,
9 Catal. Lett., 8 (1991) 27-36.
- 10 [41] R. A. Spurr, H. Myers, Quantitative Analysis of Anatase-Rutile Mixtures with an X-
11 Ray Diffractometer, Anal. Chem., 29 (1957) 760-762.
- 12 [42] P. Li, J. Liu, N. Nag, P. A. Crozier, Dynamic Nucleation and Growth of Ni
13 Nanoparticles on High-Surface Area Titania, Surf. Sci., 600 (2006) 693-702.
- 14 [43] S.-W. Ho, C.-Y. Chu, S.-G. Chen, Effect of Thermal Treatment on the Nickel State
15 and CO Hydrogenation Activity of Titania-Supported Nickel Catalysts, J. Catal., 178
16 (1998) 34-48.
- 17 [44] F.C. Meunier, On the contamination with nickel and nickel tetracarbonyl during FT-IR
18 investigation of catalysts under CO-containing gases, J. Catal., 372 (2019) 388-388.
- 19 [45] M. C. Biesinger, B. P. Payne, L. W. M. Lau, A. Gerson, R. S. C. Smart, X-ray
20 Photoelectron Spectroscopic Chemical State Quantification of Mixed Nickel Metal,
21 Oxide and Hydroxide Systems, Surf. Interface Anal., 41 (2009) 324-332.
- 22 [46] M. C. Biesinger, B. P. Payne, A. P. Grosvenor, L. W. M. Lau, A. R. Gerson, R. S. C.
23 Smart, Resolving Surface Chemical States in XPS Analysis of First Row Transition
24 Metals, Oxides and Hydroxides: Cr, Mn, Fe, Co and Ni, Appl. Surf. Sci., 257 (2011)
25 2717-2730.

- 1 [47] L. Soriano, I. Preda, A. Gutiérrez, S. Palacín, M. Abbate, A. Vollmer, Surface Effects
2 in the Ni 2p X-Ray Photoemission Spectra of NiO, *Phys. Rev. B*, 75 (2007) 233417.
- 3 [48] B. Zhao, X.-K. Ke, J.-H. Bao, C.-L. Wang, L. Dong, Y.-W. Chen, H.-L. Chen,
4 Synthesis of Flower-Like NiO and Effects of Morphology on Its Catalytic Properties,
5 *J. Phys. Chem. C*, 113, (2009) 14440-14447.
- 6 [49] V. Vonk, N. Khorshidi, A. Stierle, Structure and Oxidation Behavior of Nickel
7 Nanoparticles Supported by YSZ(111), *J. Phys. Chem. C*, 121 (2017) 2798-2806.
- 8 [50] J. Li, Y. Lin, X. Pan, D. Miao, D. Ding, Y. Cui, J. Dong, X. Bao, Enhanced CO₂
9 Methanation Activity of Ni/Anatase Catalyst by Tuning Strong Metal – Support
10 Interactions, *ACS Catal.* 9 (2019) 6342-6348.
- 11 [51] V. Nichele, M. Signoretto, F. Menegazzo, I. Rossetti, G. Cruciani, Hydrogen
12 production by ethanol steam reforming: Effect of the Synthesis Parameters on the
13 Activity of Ni/TiO₂ Catalysts, *Int. J. Hydrogen Energ.*, 39 (2014) 4252-4258.
- 14 [52] I. Rossetti, J. Lasso, E. Finocchio, G. Ramis, V. Nichele, M. Signoretto, A. Di
15 Michele, TiO₂-Supported Catalysts for the Steam Reforming of Ethanol, *Appl. Catal.*
16 *A*, 477 (2014) 42-53.
- 17 [53] X. Li, J. Lin, L. Li, Y. Huang, X. Pan, S. E. Collins, Y. Ren, Y. Su, L.i Kang, X. Liu,
18 Y. Zhou, H. Wang, A. Wang, B. Qiao, X. Wang, Tao Zhang, Controlling CO₂
19 Hydrogenation Selectivity by Metal-Supported Electron Transfer, *Angew. Chem. Int.*
20 *Ed.* 59 (2020) 19983-19989.
- 21 [54] C. Rivera-Cárcamo, C. Scarfiello, A. B. García, Y. Tison, H. Martinez, W. Baaziz, O.
22 Ersen, C. Le Berre, P. Serp, Stabilization of Metal Single Atoms on Carbon and TiO₂
23 Supports for CO₂ Hydrogenation: The Importance of Regulating Charge Transfer,
24 *Adv. Mater. Interfaces*, (2020) doi.org/10.1002/admi.202001777.

- 1 [55] M. J. Jackman, A. G. Thomas, C. Muryn, Photoelectron Spectroscopy Study of
2 Stoichiometric and Reduced Anatase TiO₂(101) Surfaces: The Effect of Subsurface
3 Defects on Water Adsorption at Near-Ambient Pressures, *J. Phys. Chem. C*, 119
4 (2015) 13682-13690.
- 5 [56] I. Ro, J. Resasco, P. Christopher, Approaches for Understanding and Controlling
6 Interfacial Effects in Oxide-Supported Metal Catalysts, *ACS Catal.*, 8 (2018) 7368-
7 7387.
- 8 [57] B. Yan, B. Zhao, S. Kattel, Q. Wu, S. Yao, D. Su, J. G. Chen, Tuning CO₂
9 Hydrogenation Selectivity via Metal-Oxide Interfacial Sites, *J. Catal.* 374 (2019) 60-
10 71.
- 11 [58] S. Kattel, P. Liu, J. G. Chen, Tuning Selectivity of CO₂ Hydrogenation Reactions at the
12 Metal/Oxide Interface, *J. Am. Chem. Soc.*, 139 (2017) 9739-9754.
- 13 [59] C. Vogt, E. Groeneveld, G. Kamsma, M. Nachtegaal, L. Lu, C. J. Kiely, P. H. Berben,
14 F. Meirer, B. M. Weckhuysen, Unravelling Structure Sensitivity in CO₂ Hydrogenation
15 over Nickel, *Nat. Catal.*, 1 (2018) 127-134.
- 16 [60] M.-M. Millet, G. Algara-Siller, S. Wrabetz, A. Mazheika, F. Girgsdies, D. Teschner, F.
17 Seitz, A. Tarasov, S. V. Levchenko, R. Schlögl, E. Frei, Ni Single Atom Catalysts for
18 CO₂ Activation, *J. Am. Chem. Soc.*, 141 (2019)) 2451-2461.
- 19 [61] C. Mebrahtu, S. Perathoner, G. Giorgianni, S. Chen, G. Centi, F. Krebs, R. Palkovits,
20 S. Abate, Deactivation Mechanism of Hydrotalcite-Derived Ni-AlO_x Catalysts during
21 Low-Temperature CO₂ Methanation via Ni-Hydroxide Formation and the Role of Fe in
22 Limiting this Effect, *Catal. Sci. Technol.*, 9 (2019) 4023-4035.
- 23 [62] A. Kokka, T. Ramantani, A. Petala, P. Panagiotopoulou, Effect of the Nature of the
24 Support, Operating and Pretreatment Conditions on the Catalytic Performance of

- 1 Supported Ni Catalysts for the Selective Methanation of CO, *Catal. Today*, (2019)
2 doi:<https://doi.org/10.1016/j.cattod.2019.04.015>.
- 3 [63] A. Karelovic, P. Ruiz, Mechanistic Study of Low Temperature CO₂ Methanation over
4 Rh/TiO₂ Catalysts, *J. Catal.*, 301 (2013) 141-153.
- 5 [64] X. Wang, Y. Hong, H. Shi, J. Szanyi, Kinetic Modeling and Transient DRIFTS-MS
6 Studies of CO₂ Methanation over Ru/Al₂O₃ catalysts, *J. Catal.* 343 (2016) 185-195.
- 7 [65] R. A. Hubble, J. Y. Lim, J. S. Dennis, Kinetic Studies of CO₂ Methanation over a
8 Ni/g-Al₂O₃ Catalyst, *Faraday Discuss.*, 192 (2016) 529-544.
- 9 [66] A. Westermann, B. Azambre, M.C. Bacariza, I. Graça, M.F. Ribeiro, J.M. Lopes, C.
10 Henriques, Insight into CO₂ Methanation Mechanism over NiUSY Zeolites: An
11 Operando IR Study, *Appl. Catal. B*, 174-175 (2015) 120-125.
- 12 [67] E. Baumgarten, G. Meyer, Hydrogen Spillover Through the Gas Phase. Some Kinetic
13 Aspects. *React. Kinet., Catal. Lett.*, 71 (2000) 325-333.
- 14 [68] E.; Baumgarten, R. Krupp, Hydrogenation of Hexene1 by Gas Phase Spillover
15 Hydrogen. Influence of Substances Added in the Reaction Chamber, Without Contact
16 to the Catalyst, *React. Kinet. Catal. Lett.*, 70 (2000) 35-41.
- 17 [69] R. Prins, Hydrogen Spillover. Facts and Fiction, *Chem. Rev.*, 112 (2012) 2714-2738.
- 18 [70] A. Karelovic, P. Ruiz, Improving the Hydrogenation Function of Pd/ γ -Al₂O₃ Catalyst
19 by Rh/ γ -Al₂O₃ Addition in CO₂ Methanation at Low Temperature, *ACS Catal.*, 3
20 (2013) 2799-2812.
- 21 [71] C. Swalusa, M. Jacquemin, C. Poleunis, P. Bertrand, P. Ruiz CO₂ Methanation on
22 Rh/ γ -Al₂O₃ Catalyst at Low Temperature: "In Situ" Supply of Hydrogen by
23 Ni/Activated Carbon Catalyst, *Appl. Catal. B*, 125 (2012) 41-50.
- 24 [72] T. Inui, Highly Effective Conversion of Carbon Dioxide to Valuable Compounds on
25 Composite Catalysts, *Catal. Today*, 29 (1996) 329-337.

- 1 [73] S. K. Beaumont, S. Alayoglu, C. Specht, N. Kruse, G. A. Somorjai, Nanoscale
2 Demonstration of Hydrogen Atom Spillover and Surface Diffusion Across Silica
3 Using the Kinetics of CO₂ Methanation Catalyzed on Spatially Separate Pt and Co
4 Nanoparticles, *Nano Lett.*, 14 (2014) 4792-4796.
- 5 [74] S. K. Beaumont, S. Alayoglu, C. Specht, W. D. Michalak, V. V. Pushkarev, J. Guo, N.
6 Kruse, G. A. Somorjai, Combining in Situ NEXAFS Spectroscopy and CO₂
7 Methanation Kinetics To Study Pt and Co Nanoparticle Catalysts Reveals Key
8 Insights into the Role of Platinum in Promoted Cobalt Catalysis, *J. Am. Chem. Soc.*,
9 136 (2014) 9898-9901.
- 10 [75] Z Yan, Q. Liu, L. Liang, J. Ouyang, Surface hydroxyls mediated CO₂ methanation at
11 ambient pressure over attapulgite-loaded Ni-TiO₂ composite catalysts with high
12 activity and reuse ability, *J. CO₂ Utilization*, 47 (2021) 101489.
- 13 [76] Y. Guo, S. Mei, K. Yuan, D.-J. Wang, H.-C. Liu, C.-H. Yan, Y.-W. Zhang, Low-
14 Temperature CO₂ Methanation over CeO₂-Supported Ru Single Atoms, Nanoclusters,
15 and Nanoparticles Competitively Tuned by Strong Metal–Support Interactions and H-
16 Spillover Effect, *ACS Catal.*, 8 (2018) 6203-6215.
- 17 [77] J. Huang, X. Li, X. Wang, X. Fang, H. Wang, X. Xu, New Insights into CO₂
18 Methanation Mechanisms on Ni/MgO Catalysts by DFT Calculations: Elucidating Ni
19 and MgO Roles and Support Effects, *J. CO₂ Util.*, 33 (2019) 55-63.
- 20 [78] G Hu, Z. Wu, D.-e. Jiang, First Principles Insight into H₂ Activation and Hydride
21 Species on TiO₂ Surfaces, *J. Phys. Chem. C*, 122 (2018) 20323-20328.
- 22 [79] R.n Wang, H. Fan, The mechanism of H₂ and H₂O desorption from bridging hydroxyls
23 of a TiO₂(110) surface, *Catal. Sci. Technol.*, 7 (2017) 251-264.

- 1 [80] W. Lin, H. Cheng, L. He, Y. Yu, F. Zhao, High Performance of Ir-Promoted Ni/TiO₂
2 Catalyst toward the Selective Hydrogenation of Cinnamaldehyde, *J. Catal.*, 303 (2013)
3 110-116.
- 4 [81] P. Panagiotopoulou, D. I. Kondarides, Effects of Alkali Additives on the
5 Physicochemical Characteristics and Chemisorptive Properties of Pt/TiO₂ Catalysts, *J.*
6 *Catal.*, 260 (2008) 141-149.
- 7 [82] P. Panagiotopoulou, D. I. Kondarides, Effects of Promotion of TiO₂ with Alkaline
8 Earth Metals on the Chemisorptive Properties and Water–Gas Shift Activity of
9 Supported Platinum Catalysts, *App. Catal. B*, 101 (2011) 738-746.
- 10 [83] Z. He, M. Hu, X. Wang, Highly Effective Hydrodeoxygenation of Guaiacol on
11 Pt/TiO₂: Promoter Effects, *Catal. Today*, 302 (2018) 136-145.
- 12 [84] X.-L. Yin, M. Calatayud, H. Qiu, Y. Wang, A. Birkner, C. Minot, C. Wöll, Diffusion
13 versus Desorption: Complex Behavior of H Atoms on an Oxide Surface,
14 *ChemPhysChem*, 9 (2008) 253-256.
- 15 [85] M. M. Islam, M. Calatayud, G. Pacchioni, Hydrogen Adsorption and Diffusion on the
16 Anatase TiO₂(101) Surface: A First-Principles Investigation, *J. Phys. Chem. C*, 115
17 (2011) 6809.
- 18 [86] S.-C. Li, Z. Zhang, D. Sheppard, B. D. Kay, J. M. White, Y. Du, I. Lyubinetsky, G.
19 Henkelman, Z. Dohnálek, Intrinsic Diffusion of Hydrogen on Rutile TiO₂(110), *J. Am.*
20 *Chem. Soc.*, 130 (2008) 9080-9088.
- 21 [87] K. Liu, P. Yan, H. Jiang, Z. Xia, Z. Xu, S. Bai, Z. C. Zhang, Silver Initiated Hydrogen
22 Spillover on Anatase TiO₂ Creates Active Sites for Selective Hydrodeoxygenation of
23 Guaiacol, *J. Catal.*, 369 (2019) 396-404.

- 1 [88] C.g Mao, J. Wang, Y. Zou, G. Qi, J. Yi, Y. Loh, T. Zhang, M. Xia, J. Xu, F. Deng, M.
2 Ghossoub, N. P. Kherani, L. Wang, H. Shang, M. Li, J. Li, X. Liu, Z. Ai, G. A. Ozin,
3 J. Zhao, L. Zhang, *J. Am. Chem. Soc.*, 142 (2020), 17403-17412.
- 4 [89] E. Baumgarten, R. Krupp, Gas Phase Hydrogen Spillover and Oxygen Content, *React.*
5 *Kinet. Catal. Lett.*, 70 (2000) 27-33.
- 6 [90] I. A. Razzhivina, G. A. Badun, M. G. Chernysheva, A. V. Garshev, V. P. Shevchenko,
7 K. V. Shevchenko, I. Y. Nagaev, N. E. Shchepina, Hydrogen Spillover through a Gas
8 Phase, *Mendeleev Commun*, 26 (2016) 59-60.
- 9 [91] E. Baumgarten, L. Maschke, Hydrogen Spillover through the Gas Phase: Reaction
10 with Graphite and Activated Carbon, *Appl. Catal. A*, 202 (2000) 171-177.
- 11 [92] M. S. Spencer, R. Burch, S. E. Golunski, Comments on “Hydrogen Spillover through
12 Gas Phase Transport of Hydrogen Atoms”, *J. Catal.*, 126 (1990) 311-313.
- 13 [93] S. S. Han, H. Kim, N. Park, Effect of Shuttling Catalyst on the Migration of Hydrogen
14 Adatoms: A Strategy for the Facile Hydrogenation of Graphene, *J. Phys. Chem. C*,
15 115 (2011) 24696-24701.
- 16 [94] Y. Zhu, D. Liu, M. Meng, H₂ Spillover Enhanced Hydrogenation Capability of TiO₂
17 Used for Photocatalytic Splitting of Water: a Traditional Phenomenon for New
18 Applications, *Chem. Commun.*, 50 (2014) 6049-6051.
- 19 [95] D. Panayotov, E. Ivanova, M. Mihaylov, K. Chakarova, T. Spassov, K. Hadjiivanov,
20 Hydrogen Spillover on Rh/TiO₂: the FTIR Study of Donated Electrons, co-Adsorbed
21 CO and H/D Exchange, *Phys. Chem. Chem. Phys.*, 17 (2015) 20563-20573.
- 22 [96] W. Wan, X. Nie, M. J. Janik, C. Song, X. Guo, Adsorption, Dissociation, and
23 Spillover of Hydrogen over Au/TiO₂ Catalysts: The Effects of Cluster Size and
24 Metal–Support Interaction from DFT, *J. Phys. Chem. C*, 122 (2018) 17895-17916.

- 1 [97] E. S. Putna, R. J. Gorte, J. M. Vohs, G. W. Grahamy, Evidence for Enhanced
2 Dissociation of CO on Rh/Ceria, *J. Catal.*, 178 (1998) 598-603.
- 3 [98] R. Burch, A. R. Flambard, Strong Metal-Support Interactions in Nickel-Titania
4 Catalysts: The Importance of Interfacial Phenomena, *J. Catal.*, 78 (1982) 389-405.
- 5 [99] X. Jia, X. Zhang, N. Rui, X. Hu, C.-j. Liu, Structural Effect of Ni/ZrO₂ Catalyst on
6 CO₂ Methanation with Enhanced Activity, *Appl. Catal. B*, 244 (2019) 159-169.
- 7 [100] S. D. Senanayake, P. J. Ramírez, I. Waluyo, S. Kundu, K. Mudiyansele, Z. Liu, Z.
8 Liu, S. Axnanda, D. J. Stacchiola, J. Evans, J. A. Rodriguez, Hydrogenation of CO₂ to
9 Methanol on CeOx/Cu(111) and ZnO/Cu(111) Catalysts: Role of the Metal–Oxide
10 Interface and Importance of Ce³⁺ Sites, *J. Phys. Chem. C*, 120 (2016) 1778-1784.
- 11 [101] Sh. Lin, Z. Hao, J. Shen, X. Chang, S. Huang, M. Li, X. Ma, Enhancing the CO₂
12 methanation activity of Ni/CeO₂ via activation treatment-determined metal-support
13 interaction, *J. Energy Chem.* 59 (2021) 334-342.
- 14 [102] W. Li, H. Wang, X. Jiang, J. Zhu, Z. Liu, X. Guo, C. Song, A short review of recent
15 advances in CO₂ hydrogenation to hydrocarbons over heterogeneous catalysts, *RSC*
16 *Adv.*, 8 (2018) 7651-7669.
- 17 [103] Y. Hinuma, T. Toyao, T. Kamachi, Z. Maeno, S. Takakusagi, S. Furukawa, I.
18 Takigawa, K.-i. Shimizu, Density functional theory calculations of oxygen vacancy
19 formation and subsequent molecular adsorption on oxide surfaces, *J. Phys. Chem. C*,
20 122 (2018) 29435-29444.
- 21 [104] J. Kapicka, N. I. Jaeger, G. Schulz-Ekloff, Evidence for a hydrogen spillover effect in
22 the deposition of coke on a nickel-faujasite catalyst during syngas conversion, *Appl.*
23 *Catal. A: General*, 84 (1992) 47-55.

- 1 [105] C.-j. Liu, J. Ye, J. Jiang, Y. Pan, Progresses in the preparation of coke resistant Ni-
2 based catalyst for steam and CO₂ reforming of methane, *ChemCatChem*, 3 (2011)
3 529-541.
- 4 [106] G. E. Batley, A. Ekstrom, D. A. Johnson, Studies of topochemical heterogeneous
5 catalysis: 3. Catalysis of the reduction of metal oxides by hydrogen, *J. Catal*, 34
6 (1974) 368-375.
- 7 [107] L. Shen, J. Xu, M. Zhu, Y.-F. Han, Essential Role of the Support for Nickel-Based
8 CO₂ Methanation Catalysts, *ACS Catal.*, 10 (2020) 14581–14591.
- 9 [108] I. T. Chashechnikova, V. M. Vorotyntsev, A. V. Gette, G. I. Golodets, Effect of
10 Rutile/Anatase Ratio on Catalytic Properties of Co–TiO₂ Catalysts for Fischer-
11 Tropsch Synthesis, *React. Kinet. Catal. Lett.*, 40 (1989) 47-51.
- 12 [109] K. Shimura, T. Miyazawa, T. Hanaoka, S. Hirata Fischer–Tropsch Synthesis over
13 TiO₂ Supported Cobalt Catalyst: Effect of TiO₂ Crystal Phase and Metal Ion Loading,
14 *Appl. Catal. A*, 460-461 (2013) 8-14.

15